International Tables for Crystallography (2006). Vol. C, Chapter 7.4, pp. 653–665.

7.4. Correction of systematic errors

By N. G. Alexandropoulos, M. J. Cooper, P. Suortti and B. T. M. Willis

7.4.1. Absorption

The positions and intensities of X-ray diffraction maxima are affected by absorption, the magnitude of the effect depending on the size and shape of the specimen. Positional effects are treated as they are encountered in the chapters on experimental techniques.

In structure determination, the effect of absorption on intensity may sometimes be negligible, if the crystal is small enough and the radiation penetrating enough. In general, however, this is not the case, and corrections must be applied. They are simplest if the crystal is of a regular geometric shape, produced either through natural growth or through grinding or cutting. Expressions for reflection from and transmission through a flat plate are given in Table 6.3.3.1, for reflection from cylinders in Table 6.3.3.2, and for reflection from spheres in Table 6.3.3.3. The calculation for a crystal bounded by arbitrary plane faces is treated in Subsection 6.3.3.3.

The values of mass absorption (attenuation) coefficients required for the calculation of corrections are given as a function of the element and of the radiation in Table 4.2.4.3.

7.4.2. Thermal diffuse scattering (By B. T. M. Willis)

7.4.2.1. *Glossary of symbols*

$\hat{e}_j$	Direction cosines of $\mathbf{e}_j(\mathbf{q})$
$\mathbf{e}_j(\mathbf{q})$	Polarization vector of normal mode $(j\mathbf{q})$
$E_j(\mathbf{q})$	Energy of mode $(j\mathbf{q})$
$E_{\rm meas}$	Total integrated intensity measured under Bragg peak
E_0	Integrated intensity from Bragg scattering
E_1	Integrated intensity from one-phonon scattering
$F(\mathbf{h})$	Structure factor
$\hbar$	Planck's constant h divided by 2π
$2\pi\mathbf{h}$	Reciprocal-lattice vector
$\mathbf{H}$	Scattering vector
j	Label for branch of dispersion relation
$\mathbf{k}_0$	Wavevector of incident radiation
$\mathbf{k}$	Wavevector of scattered radiation
k_B	Boltzmann's constant
m_n	Neutron mass
m	Mass of unit cell
N	Number of unit cells in crystal
$\mathbf{q}$	Wavevector of normal mode of vibration
q_m	Radius of scanning sphere in reciprocal space
V	Volume of unit cell
$\mathbf{v}_j$	Elastic wave velocity for branch j
$\mathbf{v}_L$	Mean velocity of elastic waves
α	TDS correction factor
2θ	Scattering angle
θ_B	Bragg angle
$\left(\frac{d\sigma}{d\Omega}\right)^{(0)}$	Differential cross section for Bragg scattering
$\left(\frac{d\sigma}{d\Omega}\right)^{(1)}$	Differential cross section for one-phonon scattering
ρ	Density of crystal
$\omega_j(\mathbf{q})$	Frequency of normal mode $(j\mathbf{q})$

Thermal diffuse scattering (TDS) is a process in which the radiation is scattered inelastically, so that the incident X-ray photon (or neutron) exchanges one or more quanta of vibrational energy with the crystal. The vibrational quantum is known as a phonon, and the TDS can be distinguished as one-phonon (first-order), two-phonon (second-order), ... scattering according to the number of phonons exchanged.

The normal modes of vibration of a crystal are characterized as either acoustic modes, for which the frequency $\omega(\mathbf{q})$ goes to zero as the wavevector $\mathbf{q}$ approaches zero, or optic modes, for which the frequency remains finite for all values of $\mathbf{q}$ [see Section 4.1.1 of *IT* B (1992)]. The one-phonon scattering by the acoustic modes rises to a maximum at the reciprocal-lattice points and so is not entirely subtracted with the background measured on either side of the reflection. This gives rise to the 'TDS error' in estimating Bragg intensities. The remaining contributions to the TDS – the two-phonon and multphonon acoustic mode scattering and all kinds of scattering by the optic modes – are largely removed with the background.

It is not easy in an X-ray experiment to separate the elastic (Bragg) and the inelastic thermal scattering by energy analysis, as the energy difference is only a few parts per million. However, this has been achieved by Dorner, Burkel, Illini & Peisl (1987) using extremely high energy resolution. The separation is also possible using Mössbauer spectroscopy. Fig. 7.4.2.1 shows the elastic and inelastic components from the 060 reflection of $LiNbO_3$ (Krec, Steiner, Pongratz & Skalicky, 1984), measured with γ-radiation from a ^{57}Co Mössbauer source. The TDS makes a substantial contribution to the measured integrated intensity; in Fig. 7.4.2.1, it is 10% of the total intensity, but it can be much larger for higher-order reflections. On the other hand, for the extremely sharp Bragg peaks obtained with synchrotron radiation, the TDS error may be reduced to negligible proportions (Bachmann, Kohler, Schulz & Weber, 1985).

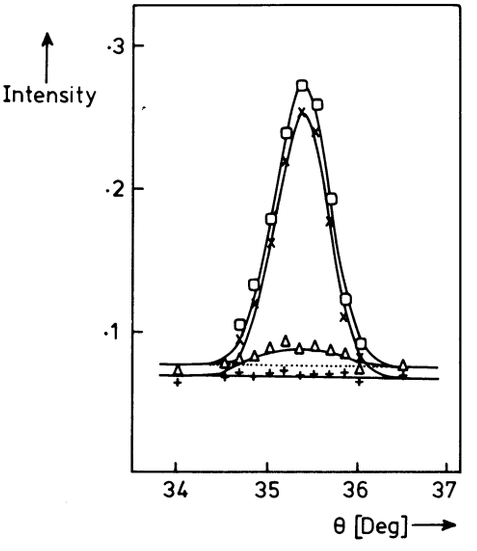

Fig. 7.4.2.1. 060 reflection of $LiNbO_3$ (Mössbauer diffraction). Inelastic (triangles), elastic (crosses), total (squares) and background (pluses) intensity (after Krec, Steiner, Pongratz & Skalicky, 1984).

Let $E_{\rm meas}$ represent the *total* integrated intensity measured in a diffraction experiment, with E_0 the contribution from Bragg scattering and E_1 that from (one-phonon) TDS. Then,

$$E_{\rm meas} = E_0 + E_1 = E_0(1+\alpha), \tag{7.4.2.1}$$

where α is the ratio E_1/E_0 and is known as the 'TDS correction factor'. α can be evaluated in terms of the properties of the crystal (elastic constants, temperature) and the experimental conditions of measurement. In the following, it is implied that the intensities are measured using a single-crystal diffractometer with incident radiation of a fixed wavelength We shall treat separately the calculation of α for X-rays and for thermal neutrons.

7.4.2.2. *TDS correction factor for X-rays (single crystals)*

The differential cross section, representing the intensity per unit solid angle for Bragg scattering, is

$$\left(\frac{{\rm d}\sigma}{{\rm d}\Omega}\right)^{(0)} = \frac{N(2\pi)^3}{V}\left|F(\mathbf{h})\right|^2\delta(\mathbf{H}-2\pi\mathbf{h}),$$

where N is the number of unit cells, each of volume V, and $F(\mathbf{h})$ is the structure factor. $\mathbf{H}$ is the scattering vector, defined by

$$\mathbf{H} = \mathbf{k} - \mathbf{k}_0,$$

with $\mathbf{k}$ and $\mathbf{k}_0$ the wavevectors of the scattered and incident beams, respectively. (The scattering is elastic, so $k = k_0 = 2\pi/\lambda$, where λ is the wavelength.) $2\pi\mathbf{h}$ is the reciprocal-lattice vector and the delta function shows that the scattered intensity is restricted to the reciprocal-lattice points.

The integrated Bragg intensity is given by

$$\begin{aligned} E_0 &= \int\int\left(\frac{{\rm d}\sigma}{{\rm d}\Omega}\right)^{(0)}{\rm d}\Omega\,{\rm d}t \\ &= N\frac{(2\pi)^3}{V}\left|F(\mathbf{h})\right|^2\int\int\delta(\mathbf{H}-2\pi\mathbf{h})\,{\rm d}\Omega\,{\rm d}t, \end{aligned} \tag{7.4.2.2}$$

where the integration is over the solid angle Ω subtended by the detector at the crystal and over the time t spent in scanning the reflection. Using

$$\int\delta(\mathbf{H})\,{\rm d}\mathbf{H} = 1,$$

with ${\rm d}\mathbf{H} = H\,{\rm d}\theta$, equation (7.4.2.2) reduces to the familiar result (James, 1962)

$$E_0 = \frac{N\lambda^3\left|F(\mathbf{h})\right|^2}{V\omega_0\sin 2\theta}, \tag{7.4.2.3}$$

where ω_0 is the angular velocity of the crystal and 2θ the scattering angle.

The differential cross section for one-phonon scattering by acoustic modes of small wavevector $\mathbf{q}$ is

$$\begin{aligned} \left(\frac{{\rm d}\sigma}{{\rm d}\Omega}\right)^{(1)} &= \frac{(2\pi)^3}{V}\left|F(\mathbf{h})\right|^2 \\ &\times\sum_{j=1}^{3}\frac{\mathbf{H}\cdot\mathbf{e}_j(\mathbf{q})}{m\omega_j^2(\mathbf{q})}E_j(\mathbf{q})\delta(\mathbf{H}\pm\mathbf{q}-2\pi\mathbf{h}) \end{aligned} \tag{7.4.2.4}$$

[see Section 4.1.1 of *IT* B (1992)]. Here, $\mathbf{e}_j(\mathbf{q})$ is the polarization vector of the mode $(j\mathbf{q})$, where j is an index for labelling the acoustic branches of the dispersion relations, m is the mass of the unit cell and $E_j(\mathbf{q})$ is the mode energy. The delta function in (7.4.2.4) shows that the scattering from the mode $(j\mathbf{q})$ is confined to the points in reciprocal space displaced by $\pm\mathbf{q}$ from the reciprocal-lattice point at $\mathbf{q}=0$. The acoustic modes involved are of small wavenumber, for which the dispersion relation can be written

$$\omega_j(\mathbf{q}) = \mathbf{v}_j\left|\mathbf{q}\right|, \tag{7.4.2.5}$$

where $\mathbf{v}_j$ is the velocity of the elastic wave with polarization vector $\mathbf{e}_j(\mathbf{q})$. Substituting (7.4.2.5) into (7.4.2.4) shows that the intensity from the acoustic modes varies as $1/q^2$, and so peaks strongly at the reciprocal-lattice points to give rise to the TDS error.

Integrating the delta function in (7.4.2.4) gives the integrated one-phonon intensity

$$\begin{aligned} E_1 &= \frac{\lambda^3}{V^2\omega_0\sin 2\theta_B}H^2\left|F(\mathbf{h})\right|^2 \\ &\times\sum_q\sum_j\frac{\left[\mathbf{H}\cdot\mathbf{e}_j(\mathbf{q})\right]^2}{\rho\omega_q^2(\mathbf{q})}E_j(\mathbf{q}), \end{aligned}$$

with ρ the crystal density. The sum over the wavevectors $\mathbf{q}$ is determined by the range of $\mathbf{q}$ encompassed in the intensity scan. The density of wavevectors is uniform in reciprocal space [see Section 4.1.1 of *IT* B (1992)], and so the sum can be replaced by an integral

$$\sum_q \rightarrow \frac{NV}{(2\pi)^3}\int{\rm d}\mathbf{q}.$$

Thus, the correction factor (E_1/E_0) is given by

$$\alpha = \frac{1}{8\pi^3}\int J(\mathbf{q})\,{\rm d}\mathbf{q}, \tag{7.4.2.6}$$

where

$$J(\mathbf{q}) = \sum_j\frac{\mathbf{H}\cdot\mathbf{e}_j(\mathbf{q})^2}{\rho\omega^2(\mathbf{q})}E_j(\mathbf{q}). \tag{7.4.2.7}$$

The integral in (7.4.2.6) is over the range of measurement, and the summation in (7.4.2.7) is over the three acoustic branches. Only long-wavelength elastic waves, with a linear dispersion relation, equation (7.4.2.5), need be considered.

7.4.2.2.1. *Evaluation of* $J(\mathbf{q})$

The frequencies $\omega_j(\mathbf{q})$ and polarization vectors $\mathbf{e}_j(\mathbf{q})$ of the elastic waves in equation (7.4.2.7) can be calculated from the classical theory of Voigt (1910) [see Wooster (1962)]. If $\widehat{e}_1$, $\widehat{e}_2$, $\widehat{e}_3$ are the direction cosines of the polarization vector with respect to orthogonal axes x, y, z, then the velocity $\mathbf{v}_j$ is determined from the elastic stiffness constants c_{ijkl} by solving the following equations of motion.

$$\begin{aligned} \widehat{e}_1\left(A_{11}-\rho v_j^2\right)+\widehat{e}_2A_{12}+\widehat{e}_3A_{13} &= 0, \\ \widehat{e}_1A_{12}+\widehat{e}_2\left(A_{22}-\rho v_j^2\right)+\widehat{e}_3A_{23} &= 0, \\ \widehat{e}_1A_{13}+\widehat{e}_2A_{23}+\widehat{e}_3\left(A_{33}-\rho v_j^2\right) &= 0. \end{aligned}$$

Here, A_{km} is the km element of a 3×3 symmetric matrix $\mathbf{A}$; if $\widehat{q}_1$, $\widehat{q}_2$, $\widehat{q}_3$ are the direction cosines of the wavevector $\mathbf{q}$ with reference to x, y, z, the km element is given in terms of the elastic stiffness constants by

$$A_{km} = \sum_{l=1}^{3}\sum_{n=1}^{3}c_{klmn}\widehat{q}_l\widehat{q}_n.$$

The four indices $klmn$ can be reduced to two, replacing 11 by 1, 22 by 2, 33 by 3, 23 and 32 by 4, 31 and 13 by 5, and 12 and 21 by 6. The elements of $\mathbf{A}$ are then given explicitly by

$$
\begin{aligned}
A_{11} &= c_{11}\widehat{q}_1^2 + c_{66}\widehat{q}_2^2 + c_{55}\widehat{q}_3^2 + 2c_{56}\widehat{q}_2\widehat{q}_3 \\
&\quad + 2c_{15}\widehat{q}_3\widehat{q}_1 + 2c_{16}\widehat{q}_1\widehat{q}_2, \\
A_{22} &= c_{66}\widehat{q}_1^2 + c_{22}\widehat{q}_2^2 + c_{44}\widehat{q}_3^2 + 2c_{24}\widehat{q}_2\widehat{q}_3 \\
&\quad + 2c_{46}\widehat{q}_3\widehat{q}_1 + 2c_{26}\widehat{q}_1\widehat{q}_2, \\
A_{33} &= c_{55}\widehat{q}_1^2 + c_{44}\widehat{q}_2^2 + c_{33}\widehat{q}_3^2 + 2c_{34}\widehat{q}_2\widehat{q}_3 \\
&\quad + 2c_{35}\widehat{q}_3\widehat{q}_1 + 2c_{45}\widehat{q}_1\widehat{q}_2, \\
A_{12} &= c_{16}\widehat{q}_1^2 + c_{26}\widehat{q}_2^2 + c_{45}\widehat{q}_3^2 + (c_{25} + c_{46})\widehat{q}_2\widehat{q}_3 \\
&\quad + (c_{14} + c_{56})\widehat{q}_3\widehat{q}_1 + (c_{12} + c_{66})\widehat{q}_1\widehat{q}_2, \\
A_{13} &= c_{15}\widehat{q}_1^2 + c_{46}\widehat{q}_2^2 + c_{35}\widehat{q}_3^2 + (c_{36} + c_{45})\widehat{q}_2\widehat{q}_3 \\
&\quad + (c_{13} + c_{55})\widehat{q}_3\widehat{q}_1 + (c_{14} + c_{56})\widehat{q}_1\widehat{q}_2, \\
A_{23} &= c_{56}\widehat{q}_1^2 + c_{24}\widehat{q}_2^2 + c_{34}\widehat{q}_3^2 + (c_{23} + c_{44})\widehat{q}_2\widehat{q}_3 \\
&\quad + (c_{36} + c_{45})\widehat{q}_3\widehat{q}_1 + (c_{25} + c_{46})\widehat{q}_1\widehat{q}_2.
\end{aligned}
$$

The setting up of the matrix $\mathbf{A}$ is a fundamental first step in calculating the TDS correction factor. This implies a knowledge of the elastic constants, whose number ranges from three for cubic crystals to twenty one for triclinic crystals. The measurement of elastic stiffness constants is described in Section 4.1.6 of *IT* B (1992).

For each direction of propagation $\widehat{\mathbf{q}}$, there are three values of ρv_j^2 $(j = 1, 2, 3)$, given by the eigenvalues of $\mathbf{A}$. The corresponding eigenvectors of $\mathbf{A}$ are the polarization vectors $\mathbf{e}_j(\mathbf{q})$. These polarization vectors are mutually perpendicular, but are not necessarily parallel or perpendicular to the propagation direction.

The function $J(\mathbf{q})$ in equation (7.4.2.7) is related to the inverse matrix $\mathbf{A}^{-1}$ by

$$J(\mathbf{q}) = \frac{k_B T}{q^2} \sum_{m=1}^{3} \sum_{n=1}^{3} \left(\mathbf{A}^{-1}\right)_{mn} H_m H_n, \tag{7.4.2.8}$$

where H_1, H_2, H_3 are the x, y, z components of the scattering vector $\mathbf{H}$, and classical equipartition of energy is assumed [$E_j(\mathbf{q}) = k_B T$]. Thus $\mathbf{A}^{-1}$ determines the anisotropy of the TDS in reciprocal space, arising from the anisotropic elastic properties of the crystal.

Isodiffusion surfaces, giving the locus in reciprocal space for which the intensity $J(\mathbf{q})$ is constant for elastic waves of a given wavelength, were first plotted by Jahn (1942). These surfaces are not spherical even for cubic crystals (unless $c_{11} - c_{12} = c_{44}$), and their shapes vary from one reciprocal-lattice point to another.

7.4.2.2.2. *Calculation of* α

Inserting (7.4.2.8) into (7.4.2.6) gives the TDS correction factor as

$$\alpha = \sum_{m=1}^{3} \sum_{n=1}^{3} T_{mn} H_m H_n, \tag{7.4.2.9}$$

where T_{mn}, an element of a 3×3 symmetric matrix $\mathbf{T}$, is defined by

$$T_{mn} = \frac{k_B T}{8\pi^3} \int \frac{\left(\mathbf{A}^{-1}\right)_{mn}}{q^2} \, \mathrm{d}\mathbf{q}. \tag{7.4.2.10}$$

Equation (7.4.2.9) can also be written in the matrix form

$$\alpha = \mathbf{H}^T \mathbf{T} \mathbf{H}, \tag{7.4.2.11}$$

with $\mathbf{H}^T = (H_1, H_2, H_3)$ representing the transpose of $\mathbf{H}$.

The components of $\mathbf{H}$ relate to orthonormal axes, whereas it is more convenient to express them in terms of Miller indices *hkl* and the axes of the reciprocal lattice. If $\mathbf{S}$ is the 3×3 matrix that transforms the scattering vector $\mathbf{H}$ from orthonormal axes to reciprocal-lattice axes, then

$$\mathbf{H} = \mathbf{S}\mathbf{h}, \tag{7.4.2.12}$$

where $\mathbf{h}^T = (h, k, l)$. The final expression for α, from (7.4.2.11) and (7.4.2.12), is

$$\alpha = \mathbf{h}^T \mathbf{S}^T \mathbf{T} \mathbf{S} \mathbf{h}. \tag{7.4.2.13}$$

This is the basic formula for the TDS correction factor.

We have assumed that the entire one-phonon TDS under the Bragg peak contributes to the measured integrated intensity, whereas some of it is removed in the background subtraction. This portion can be calculated by taking the range of integration in (7.4.2.10) as that corresponding to the region of reciprocal space covered in the background measurement.

To evaluate $\mathbf{T}$ requires the integration of the function $\mathbf{A}^{-1}$ over the scanned region in reciprocal space (see Fig. 7.4.2.2). Both the function itself and the scanned region are anisotropic about the reciprocal-lattice point, and so the TDS correction is anisotropic too, *i.e.* it depends on the direction of the diffraction vector as well as on $\sin\theta/\lambda$.

Computer programs for calculating the anisotropic TDS correction for crystals of any symmetry have been written by Rouse & Cooper (1969), Stevens (1974), Merisalo & Kurittu (1978), Helmholdt, Braam & Vos (1983), and Sakata, Stevenson & Harada (1983). To simplify the calculation, further approximations can be made, either by removing the anisotropy associated with $\mathbf{A}^{-1}$ or that associated with the scanned region. In the first case, the element T_{mn} is expressed as

$$T_{mn} = \frac{k_B T}{8\pi^3} \left\langle \left(\mathbf{A}^{-1}\right)_{mn} \right\rangle \int \frac{1}{q^2} \, \mathrm{d}q,$$

where the angle brackets indicate the average value over all directions. In the second case,

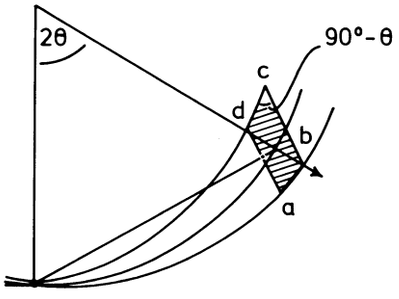

(*a*)

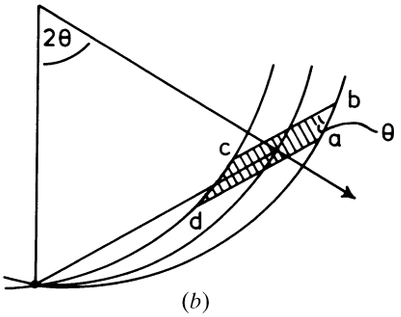

(*b*)

Fig. 7.4.2.2. Diagrams in reciprocal space illustrating the volume *abcd* swept out for (*a*) an ω scan, and (*b*) a $\theta/2\theta$, or $\omega/2\theta$, scan. The dimension of *ab* is determined by the aperture of the detector and of *bc* by the rocking angle of the crystal.

$$T_{mn} = \frac{k_B T}{8\pi^3} q_m \int\int \left(\mathbf{A}^{-1}\right)_{mn} \mathrm{d}S,$$

where q_m is the radius of the sphere that replaces the anisotropic region (Fig. 7.4.2.2) actually scanned in the experiment, and $\mathrm{d}S$ is a surface element of this sphere. q_m can be estimated by equating the volume of the sphere to the volume swept out in the scan.

If *both* approximations are employed, the correction factor is isotropic and reduces to

$$\alpha = \frac{H^2 k_B T q_m}{3\pi^2 \rho \mathbf{v}_L^2}, \qquad (7.4.2.14)$$

with $\mathbf{v}_L$ representing the mean velocity of the elastic waves, averaged over all directions of propagation and of polarization.

Experimental values of α have been measured for several crystals by γ-ray diffraction of Mössbauer radiation (Krec & Steiner, 1984). In general, there is good agreement between these values and those calculated by the numerical methods, which take into account anisotropy of the TDS. The correction factors calculated analytically from (7.4.2.14) are less satisfactory.

The principal effect of *not* correcting for TDS is to underestimate the values of the atomic displacement parameters. Writing $\exp\alpha \approx 1 + \alpha$, we see from (7.4.2.14) that the overall displacement factor is increased from B to $B + \Delta B$ when the correction is made. ΔB is given by

$$\Delta B = \frac{8 k_B T q_m}{3\pi^2 \rho \mathbf{v}_L^2}.$$

Typically, $\Delta B/B$ is 10–20%. Smaller errors occur in other parameters, but, for accurate studies of charge densities or bonding effects, a TDS correction of all integrated intensities is advisable (Helmholdt & Vos, 1977; Stevenson & Harada, 1983).

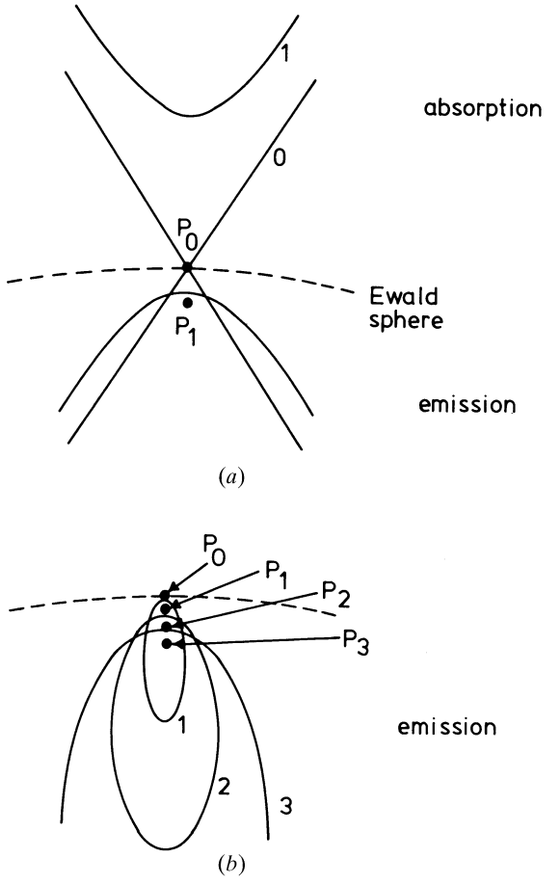

Fig. 7.4.2.3. Scattering surfaces for one-phonon scattering of neutrons: (*a*) for neutrons faster than sound ($\beta < 1$); (*b*) for neutrons slower than sound ($\beta > 1$). The scattering surface for X-rays is the Ewald sphere. P_0, P_1, *etc.* are different positions of the reciprocal-lattice point with respect to the Ewald sphere, and the scattering surfaces are numbered to correspond with the appropriate position of P.

7.4.2.3. *TDS correction factor for thermal neutrons (single crystals)*

The neutron treatment of the correction factor lies along similar lines to that for X-rays. The principal difference arises from the different topologies of the one-phonon 'scattering surfaces' for X-rays and neutrons. These surfaces represent the locus in reciprocal space of the end-points of the phonon wavevectors $\mathbf{q}$ (for fixed crystal orientation and fixed incident wavevector $\mathbf{k}_0$) when the wavevector $\mathbf{k}$ of the scattered radiation is allowed to vary. We shall not discuss the theory for pulsed neutrons, where the incident wavelength varies (see Popa & Willis, 1994).

The scattering surfaces are determined by the conservation laws for momentum transfer,

$$\mathbf{H} = \mathbf{k} - \mathbf{k}_0 = 2\pi\mathbf{h} + \mathbf{q},$$

and for energy transfer,

$$\hbar^2\left(k^2 - k_0^2\right)/2m_n = -\varepsilon\hbar\omega_j(\mathbf{q}), \qquad (7.4.2.15)$$

where m_n is the neutron mass and $\hbar\omega_j(\mathbf{q})$ is the phonon energy. ε is either $+1$ or -1, where $\varepsilon = +1$ corresponds to phonon emission (or phonon creation) in the crystal and a loss in energy of the neutrons after scattering, and $\varepsilon = -1$ corresponds to phonon absorption (or phonon annihilation) in the crystal and a gain in neutron energy. In the X-ray case, the phonon energy is negligible compared with the energy of the X-ray photon, so that (7.4.2.15) reduces to

$$k = k_0,$$

and the scattering surface is the Ewald sphere. For neutron scattering, $\hbar\omega_j(\mathbf{q})$ is comparable with the energy of a thermal neutron, and so the topology of the scattering surface is more complicated. For one-phonon scattering by long-wavelength acoustic modes with $q \ll k_0$, (7.4.2.15) reduces to

$$k = k_0 - \varepsilon\beta q,$$

where β ($= \mathbf{v}_L/\mathbf{v}_n$) is the ratio of the sound velocity in the crystal and the neutron velocity. If the Ewald sphere in the neighbourhood of a reciprocal-lattice point is replaced by its tangent plane, the scattering surface becomes a conic section with eccentricity $1/\beta$. For $\beta < 1$, the conic section is a hyperboloid of two sheets with the reciprocal-lattice point P at one focus. The phonon

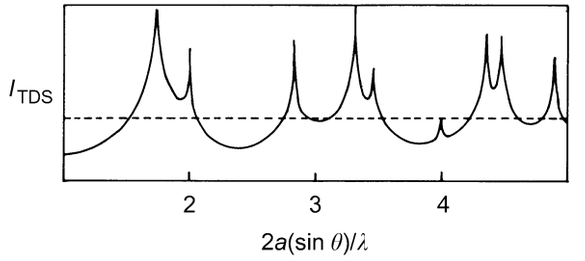

Fig. 7.4.2.4. One-phonon scattering calculated for polycrystalline nickel of lattice constant a (after Suortti, 1980).

wavevectors on one sheet correspond to scattering with phonon emission and on the other sheet to phonon absorption. For $\beta > 1$, the conic section is an ellipsoid with P at one focus. Scattering now occurs either by emission or by absorption, but not by both together (Fig. 7.4.2.3).

To evaluate the TDS correction, with **q** restricted to lie along the scattering surfaces, separate treatments are required for faster-than-sound ($\beta < 1$) and for slower-than-sound ($\beta > 1$) neutrons. The final results can be summarized as follows (Willis, 1970; Cooper, 1971):

(*a*) For faster-than-sound neutrons, the TDS rises to a maximum, just as for X-rays, and the correction factor is given by (7.4.2.13), which applies to the X-ray case. (This is a remarkable result in view of the marked difference in the one-phonon scattering surfaces for X-rays and neutrons.)

(*b*) For slower-than-sound neutrons, the correction factor depends on the velocity (wavelength) of the neutrons and is more difficult to evaluate than in (*a*). However, α will always be less than that calculated for X-rays of the same wavelength, and under certain conditions the TDS does not rise to a maximum at all so that α is then zero.

The sharp distinction between cases (*a*) and (*b*) has been confirmed experimentally using the neutron Laue technique on single-crystal silicon (Willis, Carlile & Ward, 1986).

7.4.2.4. *Correction factor for powders*

Thermal diffuse scattering in X-ray powder-diffraction patterns produces a non-uniform background that peaks sharply at the positions of the Bragg reflections, as in the single-crystal case (see Fig. 7.4.2.4). For a given value of the scattering vector, the one-phonon TDS is contributed by all those wavevectors **q** joining the reciprocal-lattice point and any point on the surface of a sphere of radius $2\sin\theta/\lambda$ with its centre at the origin of reciprocal space. These **q** vectors reach the boundary of the Brillouin zone and are not restricted to those in the neighbourhood of the reciprocal-lattice point. To calculate α properly, we require a knowledge, therefore, of the lattice dynamics of the crystal and not just its elastic properties. This is one reason why relatively little progress has been made in calculating the X-ray correction factor for powders.

7.4.3. Compton scattering
(By N. G. Alexandropoulos and M. J. Cooper)

7.4.3.1. *Introduction*

In many diffraction studies, it is necessary to correct the intensities of the Bragg peaks for a variety of inelastic scattering processes. Compton scattering is only one of the incoherent processes although the term is often used loosely to include plasmon, Raman, and resonant Raman scattering, all of which may occur in addition to the more familiar fluorescence radiation and thermal diffuse scattering. The various interactions are summarized schematically in Fig. 7.4.3.1, where the dominance of each interaction is characterized by the energy and momentum transfer and the relevant binding energy.

With the exception of thermal diffuse scattering, which is known to peak at the reciprocal-lattice points, the incoherent background varies smoothly through reciprocal space. It can be removed with a linear interpolation under the sharp Bragg peaks and without any energy analysis. On the other hand, in non-crystalline material, the elastic scattering is also diffused throughout reciprocal space; the point-by-point correction is consequently larger and without energy analysis it cannot be made empirically; it must be calculated. These calculations are imprecise except in the situations where Compton scattering is the dominant process. For this to be the case, there must be an encounter, conserving energy and momentum, between the incoming photon and an individual target electron. This in turn will occur if the energy lost by the photon, $\Delta E = E_1 - E_1$, clearly exceeds the one-electron binding energy, E_B, of the target electron. Eisenberger & Platzman (1970) have shown that this binary encounter model – alternatively known as the impulse approximation – fails as $(E_B/\Delta E)^2$.

Table 7.4.3.1. *The energy transfer, in eV, in the Compton scattering process for selected X-ray energies*

Scattering angle φ (°)	Cr $K\alpha$ 5411 eV	Cu $K\alpha$ 8040 eV	Mo $K\alpha$ 17 443 eV	Ag $K\alpha$ 22 104 eV
0	0	0	0	0
30	8	17	79	127
60	29	63	292	467
90	57	124	575	915
120	85	185	849	1344
150	105	229	1043	1648
180	112	245	1113	1757

Data calculated from equation (7.4.3.1).

The likelihood of this failure can be predicted from the Compton shift formula, which for scattering through an angle φ can be written.

$$\Delta E = E_1 - E_2 = \frac{E_1^2(1-\cos\varphi)}{mc^2[1+(E_1/mc^2)(1-\cos\varphi)]}. \qquad (7.4.3.1)$$

This energy transfer is given as a function of the scattering angle in Table 7.4.3.1 for a set of characteristic X-ray energies; it ranges from a few eV for Cr $K\alpha$ X-radiation at small angles, up to ~ 2 keV for backscattered Ag $K\alpha$ X-radiation. Clearly, in the majority of typical experiments Compton scattering will be inhibited from all but the valence electrons.

7.4.3.2. *Non-relativistic calculations of the incoherent scattering cross section*

7.4.3.2.1. *Semi-classical radiation theory*

For weak scattering, treated within the Born approximation, the incoherent scattering cross section, $(\mathrm{d}\sigma/\mathrm{d}\Omega)_{\mathrm{inc}}$, can be factorized as follows:

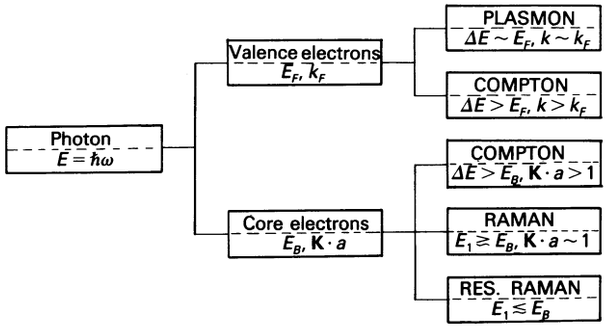

Fig. 7.4.3.1. Schematic diagram of the inelastic scattering interactions, $\Delta E = E_1 - E_2$ is the energy transferred from the photon and **K** the momentum transfer. The valence electrons are characterized by the Fermi energy, E_F, and momentum, k_F ($\hbar$ being taken as unity). The core electrons are characterized by their binding energy E_B. The dipole approximation is valid when $|\mathbf{K}|a < 1$, where a is the orbital radius of the scattering electron.

Table 7.4.3.2. *The incoherent scattering function for elements up to Z = 55*

Element	$(\sin\theta)/\lambda$ (Å^{-1})											
	0.10	0.20	0.30	0.40	0.50	0.60	0.70	0.80	0.90	1.00	1.50	2.00
1 H	0.343	0.769	0.937	0.983	0.995	0.998	0.994	0.999	1.000	1.000	1.000	1.000
2 He	0.296	0.881	1.362	1.657	1.817	1.902	1.947	1.970	1.983	1.990	1.999	2.000
3 Li	1.033	1.418	1.795	2.143	2.417	2.613	2.746	2.834	2.891	2.928	2.989	2.998
4 Be	1.170	2.121	2.471	2.744	3.005	3.237	3.429	3.579	3.693	3.777	3.954	3.989
5 B	1.147	2.531	3.190	3.499	3.732	3.948	4.146	4.320	4.469	4.590	4.895	4.973
6 C	1.039	2.604	3.643	4.184	4.478	4.690	4.878	5.051	5.208	5.348	5.781	5.930
7 N	1.08	2.858	4.097	4.792	5.182	5.437	5.635	5.809	5.968	6.113	6.630	6.860
8 O	0.977	2.799	4.293	5.257	5.828	6.175	6.411	6.596	6.755	6.901	7.462	7.764
9 F	0.880	2.691	4.347	5.552	6.339	6.832	7.151	7.376	7.552	7.703	8.288	8.648
10 Ne	0.812	2.547	4.269	5.644	6.640	7.320	7.774	8.085	8.312	8.490	9.113	9.517
11 Na	1.503	2.891	4.431	5.804	6.903	7.724	8.313	8.729	9.028	9.252	9.939	10.376
12 Mg	2.066	3.444	4.771	6.064	7.181	8.086	8.784	9.304	9.689	9.975	10.766	11.229
13 Al	2.264	4.047	5.250	6.435	7.523	8.459	9.225	9.830	10.296	10.652	11.592	12.083
14 Si	2.293	4.520	5.808	6.903	7.937	8.867	9.667	10.330	10.864	11.286	12.408	12.937
15 P	2.206	4.732	6.312	7.435	8.419	9.323	10.131	10.827	11.411	11.888	13.209	13.790
16 S	2.151	4.960	6.795	8.002	8.960	9.829	10.626	11.336	11.952	12.472	13.990	14.641
17 Cl	2.065	5.074	7.182	8.553	9.539	10.382	11.158	11.867	12.499	13.050	14.750	15.487
18 Ar	1.956	5.033	7.377	8.998	10.106	10.967	11.726	12.424	13.061	13.629	15.489	16.324
19 K	2.500	5.301	7.652	9.405	10.650	11.568	12.329	13.014	13.645	14.220	16.212	17.152
20 Ca	3.105	5.690	7.981	9.790	11.157	12.163	12.953	13.635	14.256	14.830	16.921	17.970
21 Sc	3.136	5.801	8.169	10.071	11.561	12.648	13.545	14.256	14.885	15.460	17.630	18.782
22 Ti	3.114	5.860	8.312	10.304	11.901	13.140	14.093	14.856	15.509	16.095	18.334	19.585
23 V	3.067	5.858	8.375	10.454	12.156	13.514	14.574	15.413	16.111	16.721	19.032	20.379
24 Cr	2.609	5.577	8.206	10.415	12.264	13.770	14.960	15.902	16.670	17.323	19.730	21.168
25 Mn	2.949	5.791	8.380	10.604	12.486	14.062	15.346	16.376	17.211	17.910	20.411	21.938
26 Fe	2.891	5.781	8.432	10.733	12.687	14.343	15.716	16.831	17.737	18.488	21.097	22.704
27 Co	2.832	5.764	8.469	10.844	12.867	14.596	16.050	17.249	18.229	19.039	21.777	23.462
28 Ni	2.772	5.726	8.461	10.894	12.980	14.780	16.317	17.602	18.664	19.543	22.445	24.211
29 Cu	2.348	5.455	8.310	10.778	12.942	14.847	16.494	17.885	19.043	20.002	23.107	24.957
30 Zn	2.654	5.631	8.388	10.901	13.094	15.020	16.709	18.163	19.395	20.427	23.745	25.683
31 Ga	2.791	5.939	8.599	11.082	13.290	15.233	16.947	18.445	19.734	20.831	24.370	26.400
32 Ge	2.839	6.229	8.912	11.338	13.536	15.486	17.215	18.741	20.074	21.224	24.983	27.109
33 As	2.793	6.365	9.236	11.658	13.828	15.775	17.511	19.056	20.420	21.612	25.583	27.810
34 Se	2.799	6.589	9.601	12.033	14.168	16.098	17.835	19.391	20.778	22.003	26.171	28.504
35 Br	2.771	6.748	9.940	12.440	14.552	16.456	18.185	19.747	21.149	22.399	26.747	29.190
36 Kr	2.703	6.760	10.157	12.828	14.969	16.849	18.562	20.123	21.535	22.804	27.313	29.870
37 Rb	3.225	7.062	10.431	13.206	15.410	17.282	18.974	20.526	21.940	23.221	27.871	30.543
38 Sr	3.831	7.464	10.746	13.576	15.860	17.745	19.420	20.956	22.367	23.654	28.423	31.210
39 Y	3.999	7.700	11.010	13.899	16.279	18.215	19.891	21.416	22.820	24.110	28.970	31.870
40 Zr	4.064	7.879	11.236	14.176	16.658	18.672	20.373	21.895	23.294	24.583	29.517	32.522
41 Nb	3.672	7.684	11.213	14.317	16.949	19.081	20.844	22.386	23.787	25.077	30.067	33.167
42 Mo	3.625	7.690	11.260	14.444	17.196	19.455	21.300	22.877	24.288	25.581	30.620	33.808
43 Tc	3.987	7.984	11.512	14.653	17.456	19.816	21.748	23.370	24.797	26.093	31.173	34.447
44 Ru	3.559	7.857	11.531	14.782	17.685	20.150	22.172	23.855	25.312	26.621	31.740	35.081
45 Rh	3.499	7.863	11.591	14.883	17.858	20.428	22.557	24.318	25.819	27.148	32.309	35.715
46 Pd	3.103	7.725	11.441	14.824	17.943	26.653	22.904	24.756	26.316	27.677	32.888	36.349
47 Ag	3.362	7.785	11.598	14.969	18.082	20.858	23.212	25.162	26.792	28.195	33.465	36.983
48 Cd	3.700	7.980	11.812	15.185	18.263	21.064	23.501	25.546	27.252	28.705	34.046	37.618
49 In	3.852	8.297	12.083	15.444	18.489	21.288	23.779	25.906	27.691	29.203	34.634	38.255
50 Sn	3.917	8.615	12.415	15.746	18.760	21.541	24.059	26.252	28.113	29.687	35.226	38.894
51 Sb	3.871	8.811	12.777	16.088	19.067	21.823	24.349	26.590	28.518	30.157	35.822	39.536
52 Te	3.097	9.076	13.171	16.466	19.407	22.134	25.655	26.927	28.912	30.613	36.422	40.181
53 I	3.903	9.287	13.564	16.876	19.227	22.471	24.980	27.269	29.298	31.056	37.024	40.827
54 Xe	3.841	9.340	13.892	17.307	20.175	22.833	25.324	27.619	29.680	31.488	37.628	41.477
55 Cs	4.320	9.615	14.217	17.753	20.612	23.228	25.691	27.981	30.064	31.914	38.232	42.129

$$\left(\frac{\mathrm{d}\sigma}{\mathrm{d}\Omega}\right)_{\mathrm{inc}} = \left(\frac{\mathrm{d}\sigma}{\mathrm{d}\Omega}\right)_0 S(E_1, E_2, \mathbf{K}, Z), \qquad (7.4.3.2)$$

where $(\mathrm{d}\sigma/\mathrm{d}\Omega)_0$ is the cross section characterizing the interaction, in this case it is the Thomson cross section, $(e^2/mc^2)^2\boldsymbol{\varepsilon}_1 \cdot \boldsymbol{\varepsilon}_2$; $\boldsymbol{\varepsilon}_1$ and $\boldsymbol{\varepsilon}_2$ being the initial and final state photon polarization vectors. The dynamics of the target are contained in the incoherent scattering factor $S(E_1, E_2, \mathbf{K}, Z)$, which is usually a function of the energy transfer $\Delta E = E_1 - E_2$, the momentum transfer $\mathbf{K}$, and the atomic number Z.

The electromagnetic wave perturbs the electronic system through the vector potential $\mathbf{A}$ in the Hamiltonian

$$H = \frac{e}{me}\mathbf{p}\cdot\mathbf{A} + \frac{e^2}{2me^2}\mathbf{A}\cdot\mathbf{A}. \qquad (7.4.3.3)$$

It produces photoelectric absorption through the $\mathbf{p}\cdot\mathbf{A}$ term taken in first order, Compton and Raman scattering through the $\mathbf{A}\cdot\mathbf{A}$ term and resonant Raman scattering through the $\mathbf{p}\cdot\mathbf{A}$ terms in second order.

If resonant scattering is neglected for the moment, the expression for the incoherent scattering cross section becomes

$$S = \sum_f (E_2/E_1)^2 \left| \langle \psi_f | \sum_j \exp(i\mathbf{K}\cdot\mathbf{r}_j) | \psi_i \rangle \right|^2 \delta(E_f - E_i - \Delta E), \qquad (7.4.3.4)$$

where the Born operator is summed over the j target electrons and the matrix element is summed over all final states accessible through energy conservation. In the high-energy limit of $\Delta E \gg E_B$, $S(E_1, E_2, \mathbf{K}, Z) \rightarrow Z$ but as Table 7.4.3.1 shows this condition does not hold in the X-ray regime.

The evaluation of the matrix elements in equation (7.4.3.4) was simplified by Waller & Hartree (1929) who (i) set $E_2 = E_1$ and (ii) summed over all final states irrespective of energy conservation. Closure relationships were then invoked to reduce the incoherent scattering factor to an expression in terms of form factors f_{jk}:

$$S = \sum_j [1 - |f_j(\mathbf{K})|^2] - \sum_j \sum_{k}^{j \neq k} |f_{jk}(\mathbf{K})|^2, \qquad (7.4.3.5)$$

where

$$f_j(\mathbf{K}) = \langle \psi_j | \exp(i\mathbf{K}\cdot\mathbf{r}_j) | \psi_j \rangle$$

and

$$f_{jk} = \langle \psi_k | \exp[i\mathbf{K}\cdot(\mathbf{r}_k - \mathbf{r}_j)] | \psi_j \rangle,$$

the latter term arising from exchange in the many-electron atom.

According to Currat, DeCicco & Weiss (1971), equation (7.4.3.5) can be improved by inserting the prefactor $(E_2/E_1)^2$, where E_2 is calculated from equation (7.4.3.1); the factor is an average for the factors inside the summation sign of equation (7.4.3.4) that were neglected by Waller & Hartree. This term has been included in a few calculations of incoherent intensities [see, for example, Bloch & Mendelsohn (1979)]. The Waller–Hartree method remains the chosen basis for the most extensive compilations of incoherent scattering factors, including those tabulated here, which were calculated by Cromer & Mann (1967) and Cromer (1969) from non-relativistic Hartree–Fock self-consistent-field wavefunctions. Table 7.4.3.2 is taken from the compilation by Hubbell, Veigele, Briggs, Brown, Cromer & Howerton (1975).

7.4.3.2.2. *Thomas–Fermi model*

This statistical model of the atomic charge density (Thomas, 1927; Fermi, 1928) considerably simplifies the calculation of coherent and incoherent scattering factors since both can be written as universal functions of $\mathbf{K}$ and Z. Numerical values were first calculated by Bewilogua (1931); more recent calculations have been made by Brown (1966) and Veigele (1967). The method is less accurate than Waller–Hartree theory, but it is a much simpler computation.

7.4.3.2.3. *Exact calculations*

The matrix elements of (7.4.3.4) can be evaluated exactly for the hydrogen atom. If one-electron wavefunctions in many-electron atoms are modelled by hydrogenic orbitals [with a suitable choice of the orbital exponent; see, for example, Slater (1937)], an analytical approach can be used, as was originally proposed by Bloch (1934).

Table 7.4.3.3. *Compton scattering of Mo Kα X-radiation through 170° from 2s electrons*

Element	S_{exact}	S_{imp}	$S_{\text{W–H}}$
Li	0.879	0.878	0.877
B	0.879	0.878	0.877
O	0.878	0.877	0.876
Ne	0.875	0.875	0.875
Mg	0.863	0.863	0.872
Si	0.851	0.850	0.868
Ar	0.843	0.826	0.877
V	0.663	0.716	0.875
Cr	0.568	0.636	0.875

S_{exact} is the incoherent scattering factor calculated analytically from a hydrogenic atomic model. S_{imp} is the incoherent scattering factor calculated by taking the Compton profile derived in the impulse approximation and truncating it for $\Delta E < E_B$. $S_{\text{W–H}}$ is the Waller–Hartree incoherent scattering factor. Data taken from Bloch & Mendelsohn (1974).

Hydrogenic calculations have been shown to predict accurate K- and L-shell photoelectric cross sections (Pratt & Tseng, 1972). The method has been applied in a limited number of cases to K-shell (Eisenberger & Platzman, 1970) and L-shell (Bloch & Mendelsohn, 1974) incoherent scattering factors, where it has served to highlight the deficiencies of the Waller–Hartree approach. In chromium, for example, at an incident energy of ~ 17 keV and a Bragg angle of 85°, the L-shell Waller–Hartree cross section is higher than the 'exact' calculation by $\sim 50\%$. A comparison of Waller–Hartree and exact results for 2s electrons, taken from Bloch & Mendelsohn (1974), is given in Table 7.4.3.3 for illustration. The discrepancy is much reduced when all electrons are considered.

In those instances where the exact method has been used as a yardstick, the comparison favours the 'relativistic integrated impulse approximation' outlined below, rather than the Waller–Hartree method.

7.4.3.3. *Relativistic treatment of incoherent scattering*

The Compton effect is a relativistic phenomenon and it is accordingly more satisfactory to start from this basis, *i.e.* the Klein & Nishina (1929) theory and the Dirac equation (see Jauch & Rohrlich, 1976). In second-order relativistic perturbation theory, there is no overt separation of $\mathbf{p}\cdot\mathbf{A}$ and $\mathbf{A}\cdot\mathbf{A}$ terms. The inclusion of electron spin produces additional terms in the Compton cross section that depend upon the polarization (Lipps & Tolhoek, 1954); they are generally small at X-ray energies. They are of increasing interest in synchrotron-based experiments where the brightness of the source and its polarization characteristics compensate for the small cross section (Blume & Gibbs, 1988).

Somewhat surprisingly, it is the spectral distribution, $\mathrm{d}^2\sigma/\mathrm{d}\Omega\,\mathrm{d}E_2$, rather than the total intensity, $\mathrm{d}\sigma/\mathrm{d}\Omega$, which is the better understood. This is a consequence of the exploitation of the Compton scattering technique to determine electron momentum density distributions through the Doppler broadening of the scattered radiation [see Cooper (1985) and Williams (1977) for reviews of the technique]. Manninen, Paakkari & Kajantie (1976) and Ribberfors (1975) have shown that the

Compton profile – the projection of the electron momentum density distribution onto the X-ray scattering vector – can be isolated from the relativistic differential scattering cross section within the impulse approximation. Several experimental and theoretical investigations have been concerned with understanding the changes in the spectral distribution when electron binding energies cannot be discounted. It has been found (*e.g.* Pattison & Schneider, 1979; Bloch & Mendelsohn, 1974) that, to a high degree of accuracy, the spectral distribution is merely truncated at energy transfers $E \leq E_B$.

This has led to the suggestion that the incoherent intensity can be obtained by integrating the spectral distributions, *i.e.* from

$$\frac{\mathrm{d}\sigma}{\mathrm{d}\Omega} = \int_{E_1 - E_B}^{\infty} \frac{\mathrm{d}^2\sigma}{\mathrm{d}\Omega\,\mathrm{d}E_2}\,\mathrm{d}E_2. \qquad (7.4.3.6)$$

Unfortunately, this requires the Compton profile of each electron shell as input [Compton line shapes have been tabulated by Biggs, Mendelsohn & Mann (1975)] for all elements.

Ribberfors (1983) and Ribberfors & Berggren (1982) have shown that this calculation can be dramatically simplified, without loss of accuracy, by crudely approximating the Compton line shape. Fig. 7.4.3.2 shows the incoherent scattering from aluminium, modelled in this way, and compared with experiment, Waller–Hartree theory, and an exact integral of the truncated impulse Compton profile.

7.4.3.4. *Plasmon, Raman, and resonant Raman scattering*

In typical X-ray experiments, as is evident from Table 7.4.3.1, the energy transfer may be so low that Compton scattering will be inhibited from all but the most loosely bound electrons. Indeed, in the situation in metals where $\mathbf{K}$, the momentum transfer, is less than $\mathbf{k}_F$ (the Fermi momentum), Compton scattering from the conduction electrons may be restricted by exclusion because of the lack of unoccupied final states [see Bushuev & Kuz'min (1977)]. Fortunately, in these uncertain circumstances, the incoherent intensities are low. In this regime, the electron gas may be excited into collective motion. For almost all solids, the plasmon excitation energy is 20–30 eV and, in the random phase approximation, the incoherent scattering factor becomes $S(\Delta E, K) \propto (K^2/w_p)\delta(\Delta E - h\omega_p)$, where ω_p is the plasma frequency.

At slightly higher energies ($\Delta E \geq E_B$), Compton scattering and Raman scattering can coexist, though the Raman component is only evident at low momentum transfer (Bushuev & Kuz'min, 1977). The resultant spectrum is often referred to as the Compton–Raman band. In semi-classical radiation theory, Raman scattering is usually differentiated from Compton scattering by dropping the requirement for momentum conservation between the photon and the individual target electron, the recoil being absorbed by the atom. The Raman band corresponds to transitions into the lowest unoccupied levels and these can be calculated within the dipole approximation as long as $|\mathbf{K}|a < 1$, where $\mathbf{K}$ is the momentum transfer and a the orbital radius of the core electron undergoing the transition. The transition probability in equation (7.4.3.4) becomes

$$\sum_f |\langle\psi_f|\mathbf{r}|\psi_i\rangle|^2 \delta(E_f - E_i - \Delta E), \qquad (7.4.3.7)$$

which implies that the near-edge structure is similar to the photoelectric absorption spectrum.

Whereas plasmon and Raman scattering are unlikely to make dramatic contributions to the total incoherent intensity, resonant Raman scattering (RRS) may, when $E_1 \leq E_B$. The excitation involves a virtual K-shell vacancy in the intermediate state and a vacancy in the L (or M or N) shell and an electron in the continuum in the final state. It has now been observed in a variety of materials [see, for example, Sparks (1974), Eisenberger, Platzman & Winick (1976), Schaupp *et al.* (1984)]. It was predicted by Gavrila & Tugulea (1975) and the theory has been treated comprehensively by Åberg & Tulkki (1985). The effect is the exact counterpart, in the inelastic spectrum, of anomalous

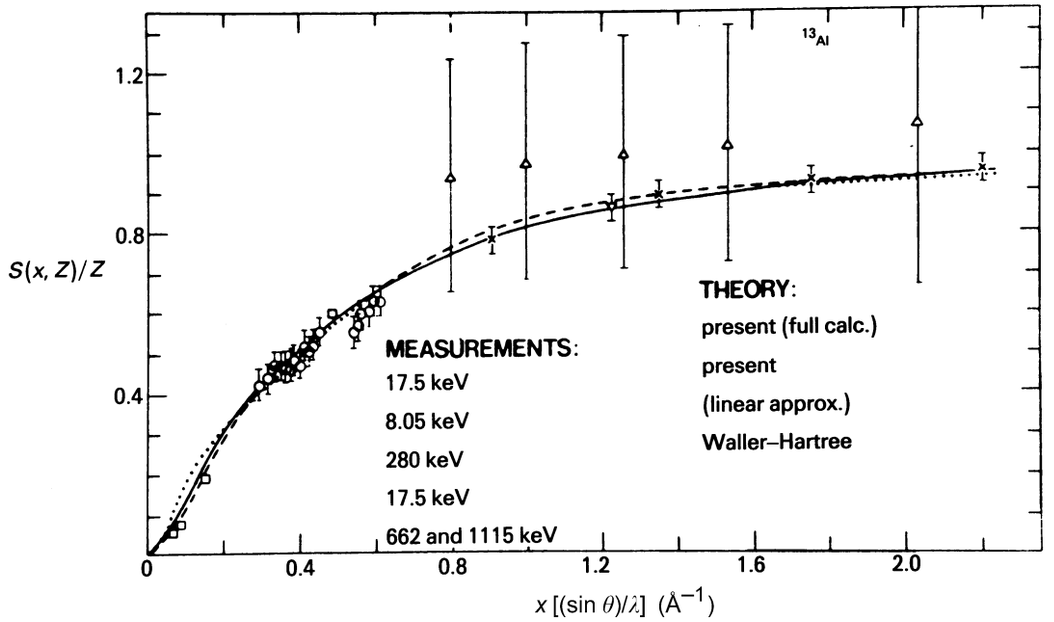

Fig. 7.4.3.2. The incoherent scattering function, $S(x, Z)/Z$, per electron for aluminium shown as a function of $x = (\sin\theta)/\lambda$. The Waller–Hartree theory (·····) is compared with the truncated impulse approximation in the tabulated Compton profiles (Biggs, Mendelsohn & Mann, 1975) cut-off at $E < E_B$ for each electron group (——). The third curve (– – –) shows the simplification introduced by Ribberfors (1983) and Ribberfors & Berggren (1982). The predictions are indistinguishable to within experimental error except at low $(\sin\theta)/\lambda$. Reference to the measurements can be found in Ribberfors & Berggren (1982).

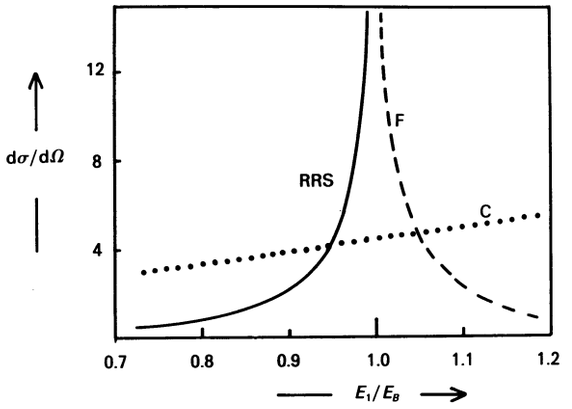

Fig. 7.4.3.3. The cross section for resonant Raman scattering (RRS) and fluorescence (F) as a function of the ratio of the incident energy, E, and the K-binding energy, E_B. The units of $d\sigma/d\Omega$ are $(e^2/mc^2)^2$ and the data are taken from Bannett & Freund (1975). For comparison, the intensity of Compton scattering (C) from copper through an angle of 30° is also shown [data taken from Hubbell *et al*. (1975)].

scattering in the elastic spectrum. It is important because, as the resonance condition is approached, the intensity will exceed that due to Compton scattering and therefore play havoc with any corrections to total intensities based solely on the latter.

Although systematic tabulations of resonance Raman scattering do not exist, Fig. 7.4.3.3, which is based on the calculations of Bannett & Freund (1975), shows how the intensity of RRS clearly exceeds that of the Compton scattering for incident energies just below the absorption edge. However, since the problems posed by anomalous scattering and X-ray fluorescence are generally appreciated, the energy range $0.9 < E_1/E_B < 1.1$ is wisely avoided by crystallographers intent upon absolute intensity measurements.

7.4.3.5. *Magnetic scattering*

Finally, and for completeness, it should be noted that the intensity of Compton scattering from a magnetic material with a net spin moment will, in principle, differ from that from a non-magnetic material. For unpolarized radiation, the effects are only discernible at photon energies greatly in excess of the electron rest mass energy, $mc^2 = 511\,\text{keV}$, but for circularly polarized radiation effects at the 1% level can be found in Compton scattering experiments carried out at $E_1 \simeq 1/10\,mc^2$ on ferromagnets such as iron. See Lipps & Tolhoek (1954) for a comprehensive description of polarization phenomena in magnetic scattering and Lovesey (1993) for an account of the scattering theory.

7.4.4. White radiation and other sources of background (By P. Suortti)

7.4.4.1. *Introduction*

By definition, the background includes everything except the signal. In an X-ray diffraction measurement, the signal is the pattern of Bragg reflections. The profiles of the reflections should be determined by the structure of the sample, and so the broadening due to the instrument should be considered as background. In the ideal angle-dispersive experiment, a well collimated beam of X-rays having a well defined energy (and a polarization, perhaps) falls on the sample, and only the radiation scattered by the sample is detected. Furthermore, the detector should be able to resolve all the components of scattering by energy, so that each scattering process could be studied separately. It is obvious that only after this kind of analysis are the Bragg reflections (plus the possible disorder scattering) unequivocally separated from the background arising from other processes. In most cases, however, this analysis is not feasible, and the reflections are separated by using certain assumptions concerning their profile, and the success of this procedure depends on the peak-to-background ratio.

The ideal situation described above is all too often not encountered, and experimenters are satisfied with too low a level of resolution. The aim of the present article is to point out the sources of the unwanted and unresolved components of the registered radiation and to suggest how these may be eliminated or resolved, so that the quality of the diffraction pattern is as high as possible. The article can cover only a few of the possible experimental situations, and only the 'almost ideal' angle-dispersive instrument is considered. It is assumed that the beam incident on the sample is monochromatized by reflection from a crystal and that the scattered radiation is registered by a low-noise quantum detector, which is the standard arrangement for modern diffractometers. Filtered radiation and photographic recording are used in certain applications, but these are excluded from the following discussion. The wavelength-dispersive or Laue methods are becoming popular at the synchrotron-radiation laboratories, and a short comment on these techniques will be included. Other sections of this volume deal with the components of scattering that are present even in the ideal experiment: thermal diffuse scattering (TDS), Compton and plasmon scattering, fluorescence and resonant Raman scattering, multiple scattering (coherent and incoherent), and disorder scattering.

The rest of the background may be termed 'parasitic' scattering, and it arises from three sources:

(1) impurities of the incident beam;
(2) impurities of the sample;
(3) surroundings of the sample.

Parasitic scattering is occasionally mentioned in the literature, but it has hardly ever been the subject of a detailed study. Therefore, the present article will discuss the general principles of the minimization of the background and then illustrate these ideas with examples. Most of the discussion will be directed to the first of the three sources of parasitic scattering, because the other two depend on the details of the experiment.

7.4.4.2. *Incident beam and sample*

An ideal diffraction experiment should be viewed as an X-ray optical system where all the parts are properly matched for the desired resolution and efficiency. The impurities of the incident beam are the wavelengths and divergent rays that do not contribute to the signal but scatter from the sample through the various processes mentioned above. The propagation of the X-ray beam through the instrument is perhaps best illustrated by the so-called phase-space analysis. The three-dimensional version, which will be used in the following, was introduced by Matsushita & Kaminaga (1980) and was elaborated further by Matsushita & Hashizume (1983). The width, divergence and wavelength range of the beam are given as a contour diagram, which originates in the X-ray source, and is modified by slits, monochromator, sample, and the detection system. The actual five-dimensional diagram is usually given as three-dimensional projections on the plane of diffraction and on the plane perpendicular to it and the beam axis, and in most cases the first projection is sufficient for an adequate description of the geometry of the experiment.

The limitations of the actual experiments are best studied through a comparison with the ideal situation. A close approximation to the ideal experimental arrangement is shown in Fig. 7.4.4.1 as a series of phase-space diagrams. The characteristic radiation from a conventional X-ray tube is almost uniformly distributed over the solid angle of 2π, and the relative width of the $K\alpha_1$ or $K\alpha_2$ emission line is typically $\Delta\lambda/\lambda = 5 \times 10^{-4}$. The acceptance and emittance windows of a flat perfect crystal are given in Fig. 7.4.4.1(*b*). The angular acceptance of the crystal (Darwin width) is typically less than 10^{-4} rad, and, if the width of the slit s or that of the crystal is small enough, none of the $K\alpha_2$ distribution falls within the window. Therefore, it is sufficient to study the size and divergence distributions of the beam in the $\lambda(K\alpha_1)$ plane only, as shown in Fig. 7.4.4.1(*c*). The beam transmitted by the flat monochromator and a slit is shown as the hatched area, and the part reflected by a small crystal by the cross-hatched area. The reflectivity curve of the crystal is probed when the crystal is rotated. In this schematic case, almost 100% of the beam contributes to the signal. The typical reflection profile shown in Fig. 7.4.4.2 reveals the details of the crystallite distribution of the sample (Suortti, 1985). The broken curve shows the calculated profile of the same reflection if the incident beam from a mosaic crystal monochromator had been used (see below).

The window of acceptance of a flat mosaic crystal is determined by the width of the mosaic distribution, which may be 100 times larger than the Darwin width of the reflection in

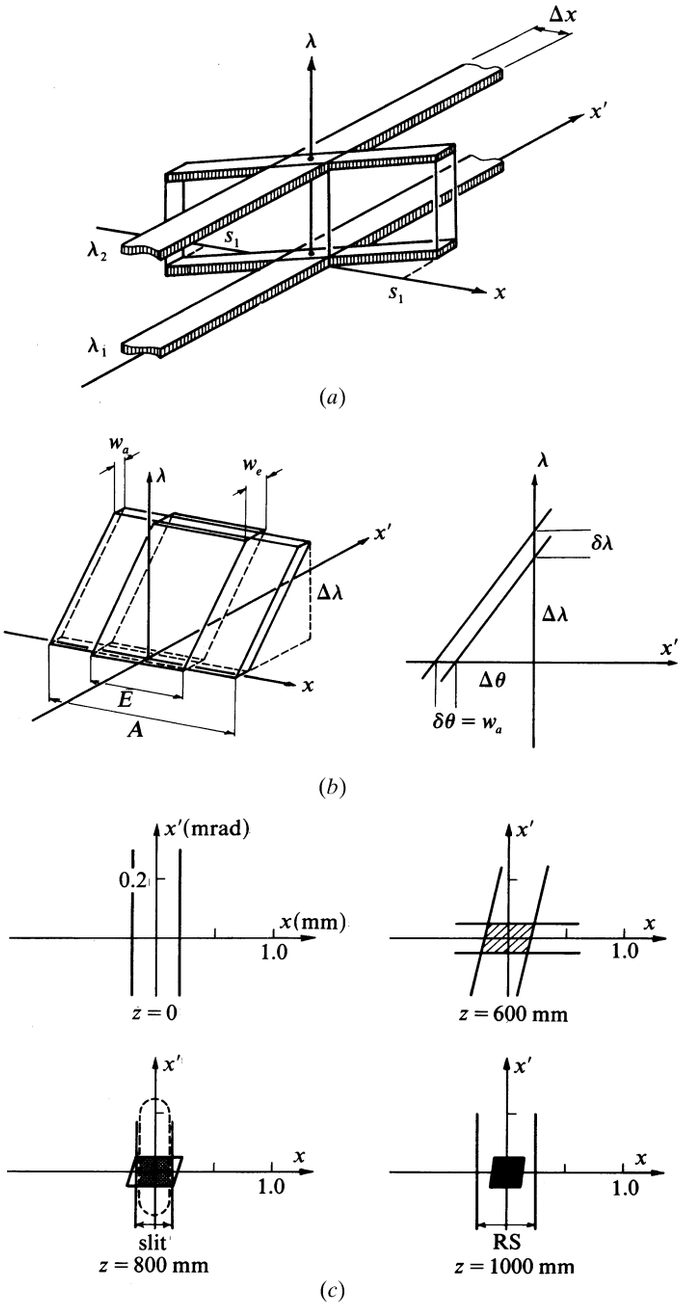

Fig. 7.4.4.1. Equatorial phase-space diagrams for a conventional X-ray source and parallel-beam geometry; x is the size and $x' = \mathrm{d}x/\mathrm{d}z$ the divergence of the X-rays. (*a*) Radiation distributions for two wavelengths, λ_1 and λ_2, at the source of width Δx, and downstream at a slit of width $\pm s_1$. (*b*) Acceptance and emittance windows of a flat perfect crystal, where the phase-space volume remains constant, $Aw_a\Delta\lambda = Ew_e\Delta\lambda$, and the (x', λ) section shows the reflection of a polychromatic beam (Laue diffraction). (*c*) Distributions for one wavelength at the source, flat perfect-crystal monochromator, sample (marked with the broken line), and the receiving slit (RS); z is the distance from the source.

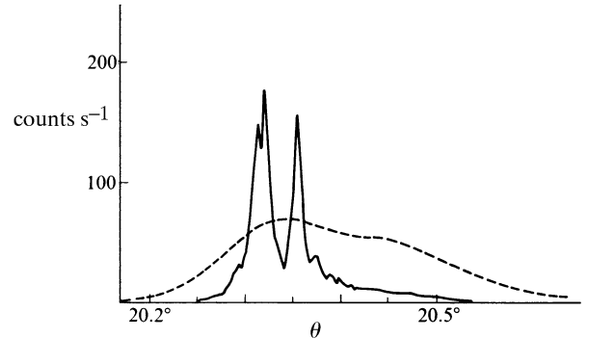

Fig. 7.4.4.2. Reflection 400 of LiH measured with a parallel beam of Mo $K\alpha_1$ radiation (solid curve). The broken curve shows the reflection as convoluted by a Gaussian instrumention function of $2\sigma = 0.1^\circ$ and $\theta(\alpha_2) - \theta(\alpha_1) = 0.13^\circ$, which values are comparable with those in Fig. 7.4.4.4.

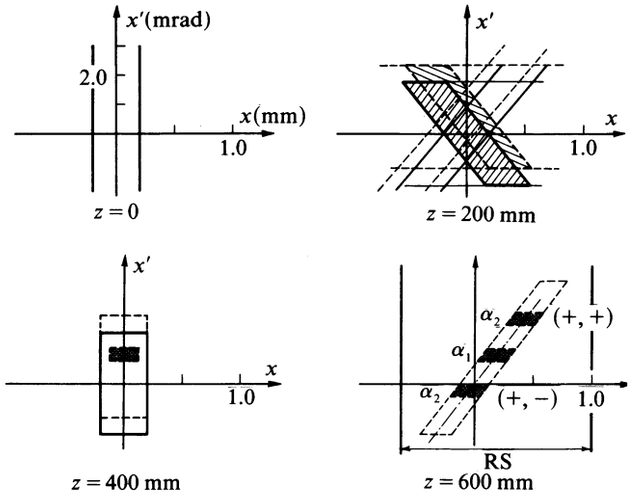

Fig. 7.4.4.3. Equatorial phase-space diagrams for two wavelengths, λ_1 (solid lines) and λ_2 (broken lines), projected on the plane $\lambda = \lambda_1$. The monochromator at $z = 200$ mm is a flat mosaic crystal, and a small sample is located at $z = 400$ mm, as shown by the shaded area. The reflected beams at the receiving slit are shown for the $(+, +)$ and $(+, -)$ configurations of the monochromator and the sample.

question. This means that a convergent beam is reflected in the same way as from a bent perfect crystal in Johann or Johansson geometry. Usually, the window is wide enough to transmit an energy band that includes both $K\alpha_1$ and $K\alpha_2$ components of the incident beam. The distributions of these components are projected on the (x, x', λ_1) plane in Fig. 7.4.4.3. The sample is placed in the (para)focus of the beam, and often the divergence of the beam is much larger than the width of the rocking curve of the sample crystal. This means that at any given time the signal comes from a small part of the beam, but the whole beam contributes to the background. The profile of the reflection is a convolution of the actual rocking curve with the divergence and wavelength distributions of the beam. The calculated profile in Fig. 7.4.4.2 demonstrates that in a typical case the profile is determined by the instrument, and the peak-to-background ratio is much worse than with a perfect-crystal monochromator.

An alternative arrangement, which has become quite popular in recent years, is one where the plane of diffraction at the monochromator is perpendicular to that at the sample. The beam is limited by slits only in the latter plane, and the wavelength varies in the perpendicular plane. An example of rocking curves measured by this kind of diffractometer is given in Fig. 7.4.4.4. The $K\alpha_1$ and $K\alpha_2$ components are seen separately plus a long tail due to continuum radiation, and the profile is that of the divergence of the beam.

In the Laue method, a well collimated beam of white radiation is reflected by a stationary crystal. The wavelength band reflected by a perfect crystal is indicated in Fig. 7.4.4.1(*b*). The mosaic blocks select a band of wavelengths from the incident beam and the wavelength deviation is related to the angular deviation by $\Delta\lambda/\lambda = \cot\theta\Delta\theta$. The angular resolution is determined by the divergences of the incident beam and the spatial resolution of the detector. The detector is not energy dispersive, so that the background arises from all scattering that reaches the detector. An estimate of the background level involves integrations over the incident spectrum at a fixed scattering angle, weighted by the cross sections of inelastic scattering and the attenuation factors. This calculation is very complicated, but at any rate the background level is far higher than that in a diffraction measurement with a monochromatic incident beam.

7.4.4.3. *Detecting system*

The detecting system is an integral part of the X-ray optics of a diffraction experiment, and it can be included in the phase-space diagrams. In single-crystal diffraction, the detecting system is usually a rectangular slit followed by a photon counter, and the slit is large enough to accept all the reflected beam. The slit can be stationary during the scan (ω scan) or follow the rotation of the sample ($\omega/2\theta$ scan). The included TDS depends on these choices, but otherwise the amount of background is proportional to the area of the receiving slit. It is obvious from a comparison between Fig. 7.4.4.1 and Fig. 7.4.4.3 that a much smaller receiving slit is sufficient in the parallel-beam geometry than in the conventional divergent-beam geometry. Mathieson (1985) has given a thorough analysis of various monochromator–sample–detector combinations and has suggested the use of a two-dimensional $\omega/2\theta$ scan with a narrow receiving slit. This provides a deconvolution of the reflection profile measured with a divergent beam, but the same result with better intensity and resolution is obtained by the parallel-beam techniques.

The above discussion has concentrated on improving the signal-to-background ratio by optimization of the diffraction geometry. This ratio can be improved substantially by an energy-dispersive detector, but, on the other hand, all detectors have some noise, which increases the background. There have been marked developments in recent years, and traditional technology has been replaced by new constructions. Much of this work has been carried out in synchrotron-radiation laboratories (for

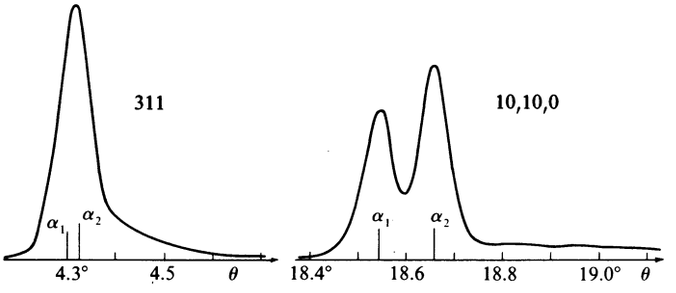

Fig. 7.4.4.4. Two reflections of beryllium acetate measured with Mo $K\alpha$. The graphite (002) monochromator reflects in the vertical plane, while the crystal reflects in the horizontal plane. The equatorial divergence of the beam is 0.8°, FWHM.

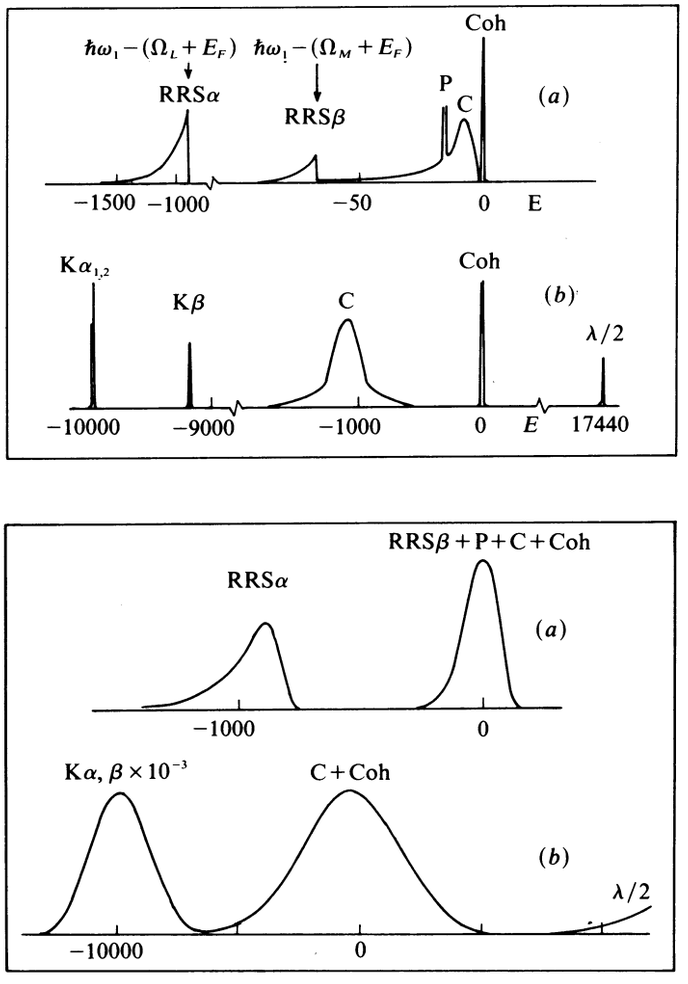

Fig. 7.4.4.5. Components of scattering at small scattering angles when the incident energy is just below the *K* absorption edge of the sample [upper part, (*a*)], and at large scattering angles when the incident energy is about twice the *K*-edge energy [upper part, (*b*)]. The abbreviations indicate resonant Raman scattering (RRS), plasmon (P) and Compton (C) scattering, coherent scattering (Coh) and sample fluorescence ($K\alpha$ and $K\beta$). The lower part shows these components as convoluted by the resolution function of the detector: (*a*) a SSD and (*b*) a scintillation counter (Suortti, 1980).

references, see Thomlinson & Williams, 1984; Brown & Lindau, 1986).

A position-sensitive detector can replace the receiving slit when a reciprocal space is scanned. TV area detectors with an X-ray-to-visible light converter and two-dimensional CCD arrays have moderate resolution and efficiency, but they work in the current mode and do not provide pulse discrimination on the basis of the photon energy. One- and two-dimensional proportional chambers have a spatial resolution of the order of 0.1 mm, and the relative energy resolution, $\Delta E/E \simeq 0.2$, is sufficient for rejection of some of the parasitic scattering.

The NaI(Tl) scintillation counter is used most frequently as the X-ray detector in crystallography. It has 100% efficiency for the commonly used wavelengths, and the energy resolution is comparable to that of a proportional counter. The detector has a long life, and the level of the low-energy noise can be reduced to about 0.1 counts s^{-1}.

The Ge and Si(Li) solid-state detectors (SSD) have an energy resolution $\Delta E/E = 0.01$ to 0.03 for the wavelengths used in crystallography. The relative Compton shift, $\Delta\lambda/\lambda$, is $(0.024\ \text{Å}/\lambda) \times (1 - \cos 2\theta)$, where 2θ is the scattering angle, so that even this component can be eliminated to some extent by a SSD. These detectors have been bulky and expensive, but new constructions that are suitable for X-ray diffraction have become available recently. The effects of the detector resolution are shown schematically in Fig. 7.4.4.5 for a scintillation counter and a SSD.

Crystal monochromators placed in front of the detector eliminate all inelastic scattering but the TDS. The monochromator must be matched with the preceding X-ray optical system, the sample included, and therefore diffracted-beam monochromators are used in powder diffraction only (see Subsection 7.4.4.4).

7.4.4.4. *Powder diffraction*

The signal-to-background ratio is much worse in powder diffraction than in single-crystal diffraction, because the background is proportional to the irradiated volume in both cases, but the powder reflection is distributed over a ring of which only the order of 1% is recorded. The phase-space diagrams of a typical measurement are shown in Fig. 7.4.4.6. The Johansson monochromator is matched to the incident beam to provide

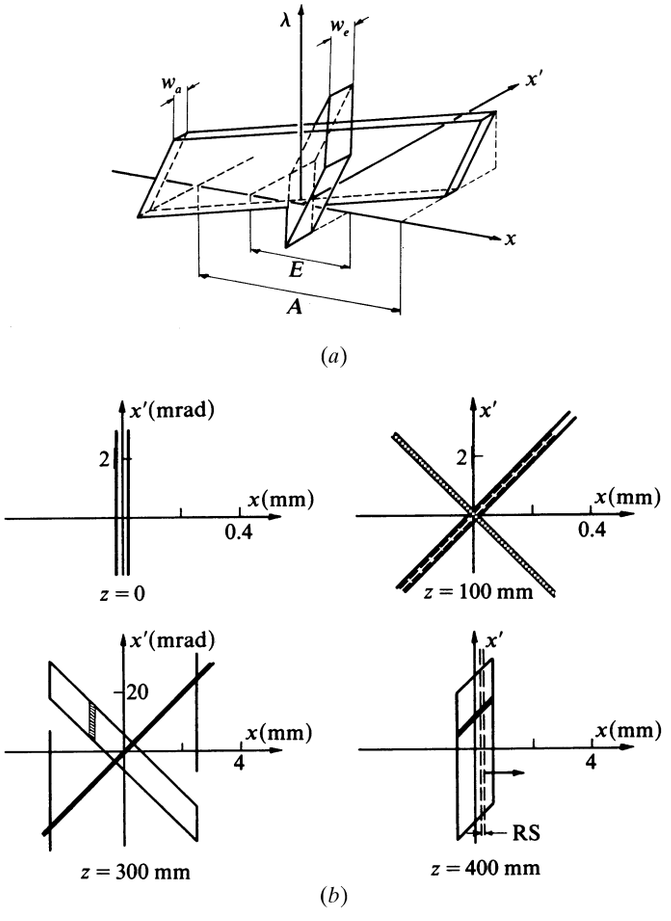

Fig. 7.4.4.6. Equatorial phase-space diagrams for powder diffraction in the Bragg–Brentano geometry. (*a*) The acceptance and emittance windows of a Johannson monochromator; (*b*) the beam in the $\lambda = \lambda_1$ plane: the exit beam from the Johansson monochromator is shown by the hatched area ($z = 100$ mm), the beam on the sample by two closely spaced lines, the reflectivity range of powder particles in a small area of the sample by the hatched area ($z = 300$ mm, note the change of scales), and the scan of the reflected beam by a slit RS by broken lines ($z = 400$ mm, at the parafocus).

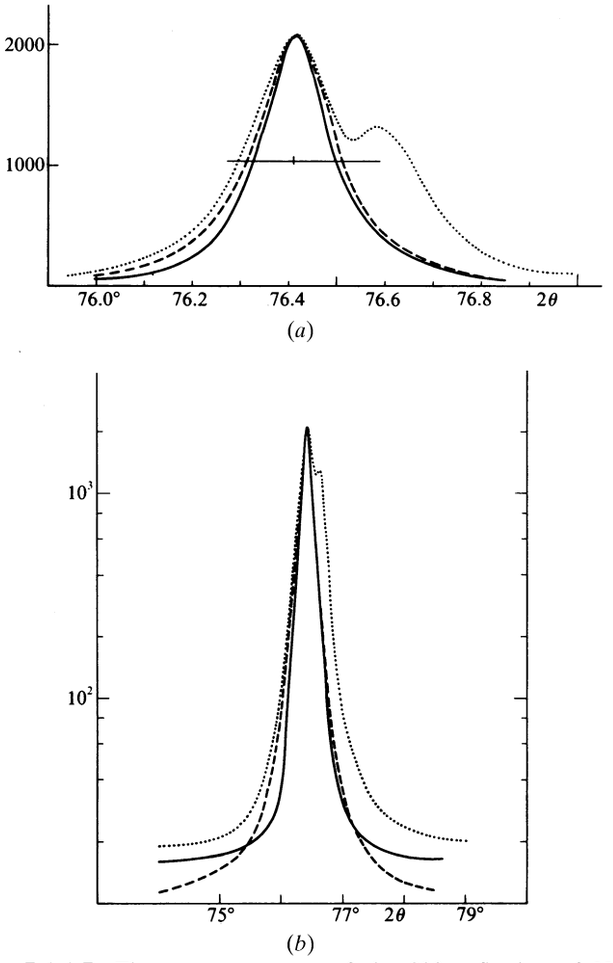

Fig. 7.4.4.7. Three measurements of the 220 reflection of Ni at $\lambda = 1.541$ Å scaled to the same peak value; (*a*) in linear scale, (*b*) in logarithmic scale. Dotted curve: graphite (00.2) Johann monochromator, conventional 0.1 mm wide X-ray source (Suortti & Jennings, 1977); solid curve: quartz (10.1) Johansson monochromator, conventional 0.05 mm wide X-ray source; broken curve: synchrotron radiation monochromatized by a (+, −) pair of Si (111) crystals, where the second crystal is sagittally bent for horizontal focusing (Suortti, Hastings & Cox, 1985). The horizontal line indicates the half-maximum value. In all cases, the effective slit width is much less than the FWHM of the reflection.

maximum flux and good energy resolution. The Bragg–Brentano geometry is parafocusing, and, if the geometrical aberrations are ignored, the reflected beam is a convolution between the angular width of the monochromator focus (as seen from the sample) and the reflectivity curve of an average crystallite of the powder sample. The profile of this function is scanned by a narrow slit, as shown in the last diagram. The slit can be followed with a Johann or Johansson monochromator that has a narrow wavelength pass-band. In this case, there is no primary-beam monochromator, so that the incident beam at the sample is that given at $z = 100$ mm. The slit RS is the 'source' for the monochromator, which focuses the beam at the detector. The obvious advantages of this arrangement are counterbalanced by certain limitations such as that the effective receiving slit is determined by the reflectivity curve of the monochromator, and this may vary over the effective area.

Examples of a powder reflection measured with different instruments and 1.5 Å radiation are given in Fig. 7.4.4.7. It should be noticed that scattering from the impurities of the sample and from the sample environment is negligible in all three cases. The width of the mosaic distribution of the 00.2 reflection of the pyrolytic graphite monochromator is 0.3°, which corresponds to a 180 eV (0.034 Å) wide transmitted beam. This is almost 10 times the separation between $K\alpha_1$ and $K\alpha_2$, and 70 times the natural width of the $K\alpha_1$ line. The width of the focal line is about 0.2 mm, or 0.07°, and is seen as broadening of the reflection profile. The quartz (10.1) monochromator reflects a band that is determined by the projected width of the X-ray source. In the present case, the band is 15 eV wide, so that the monochromator can be tuned to transmit the $K\alpha_1$ component only. The focal line is very sharp, 0.05 mm wide, and so the reflection is much narrower than in the preceding case. The third measurement was made with synchrotron radiation, and the receiving slit was replaced by a perfect-crystal analyser. The divergences of the incident and diffracted beams are about 0.1 mrad (less than 0.01°) in the plane of diffraction, so that the ideal parallel-beam geometry should prevail. However, the reflection is clearly broader than that measured with the conventional diffractometer. The reason is a wavelength gradient across the beam, which was monochromatized by a flat perfect crystal. On the other hand, the Ge (111) analyser crystal transmits elastic scattering and TDS only, and 2° away from the peak the background is 0.5% of the maximum intensity.

The above considerations may seem to have little relevance to everyday crystallographic practices. Unfortunately, many standard methods yield diffraction patterns of poor quality. The quest for maximum integrated intensity has led to designs that make reflections broad and background high. It should be realized that not the flux but the brilliance of the incident beam is important in a diffraction measurement. The other aspect is that the information should not be lost in the experiment, and a divergent wide wavelength band is quite an ignorant probe of a reflection from a single crystal.

A situation where even small departures from the ideal diffraction geometry may cause large effects is measurement at an energy just below an absorption edge. Even a small tail of the energy band of the incident beam may excite radiation that becomes the dominant component of background. Similar effects are due to the harmonic energy bands reflected by most monochromators, particularly when the continuous spectrum of synchrotron radiation is used.

Scattering from the surroundings of the sample can be eliminated almost totally by shielding and beam tunnels. The general idea of the construction should be that an optical element of the instrument 'sees' the preceding element only. Inevitably, the detector sees some of the environment of the sample. The density of air is about 1/1000 of that of a solid sample, so that 10 mm^3 of irradiated air contributes to the background as much as a spherical crystal of 0.3 mm diameter. Strong spurious peaks may arise from slit edges and entrance windows of the specimen chamber, which should never be seen by the detector. A complete measurement without the sample is always a good starting point for an experiment.

7.3 (*cont.*)

Allemand, R., Bourdel, J., Roudaut, E., Convert, P., Ibel, K., Jacobé, J., Cotton, J. P. & Farnoux, B. (1975). *Position-sensitive detectors (P.S.D.) for neutron diffraction*. *Nucl. Instrum. Methods*, **126**, 29–42.

Baruchel, J., Malgrange, C. & Schlenker, M. (1983). *Neutron diffraction topography: using position-sensitive photographic detection to investigate defects and domains in single crystals*. *Position-sensitive detection of thermal neutrons,* edited by P. Convert & J. B. Forsyth, pp. 400–406. London: Academic Press.

Berliner, R., Mildner, D. F. R., Sudol, J. & Taub, H. (1983). *Position-sensitive detectors and data collection systems at the University of Missouri Research Reactor Facility*. *Position-sensitive detection of thermal neutrons*, edited by P. Convert & J. B. Forsyth, pp. 120–128. London: Academic Press.

Boie, R. A., Fischer, J., Inagaki, Y., Merritt, F. C., Okuno, H. & Radeka, V. (1982). *Two-dimensional high precision thermal neutron detector*. *Nucl. Instrum. Methods*, **200**, 533–545.

Borkowski, C. J. & Kopp, M. K. (1975). *Design and properties of position-sensitive proportional counters using resistance-capacitance position encoding*. *Rev. Sci. Instrum.* **46**, 951–962.

Convert, P. & Chieux, P. (1986). *From BF_3 counter to PSD. An impressive and continuous increase of the data acquisition rate*. *Fifty years of neutron diffraction,* edited by G. E. Bacon, pp. 218–227. Bristol: Adam Hilger.

Convert, P. & Forsyth, J. B. (1983). *Position-sensitive detection of thermal neutrons:* Part 1, *Introduction*. *Position-sensitive detection of thermal neutrons*, pp. 1–90. London: Academic Press.

Fischer, J., Radeka, V. & Boie, R. A. (1983). *High position resolution and accuracy in ^3He two-dimensional thermal neutron PSDs*. *Position-sensitive detection of thermal neutrons*, edited by P. Convert & J. B. Forsyth, pp. 129–140. London: Academic Press.

Hohlwein, D. (1983). *Photographic methods in neutron scattering*. *Position-sensitive detection of thermal neutrons*, edited by P. Convert & J. B. Forsyth, pp. 379–390. London: Academic Press.

Ibel, K. (1976). *The neutron small-angle camera D11 at the high-flux reactor, Grenoble*. *J. Appl. Cryst.* **9**, 296–309.

Institut Laue–Langevin (1988). *Guide to neutron research facilities at the ILL*. Grenoble: Institut Laue–Langevin.

Isis (1992). *User Guide*. Didcot: Rutherford Appleton Laboratory.

Kurz, R. & Schelten, J. (1983). *Properties of various scintillators for thermal neutron detection*. *Position-sensitive detection of thermal neutrons,* edited by P. Convert & J. B. Forsyth, pp. 192–196. London: Academic Press.

Naday, I. & Schaefer, W. (1983). *A new processing method and gain stabilisation for scintillation position-sensitive detectors*. *Position-sensitive detection of thermal neutrons,* edited by P. Convert & J. B. Forsyth, pp. 197–202. London: Academic Press.

Roudaut, E. (1983). *Evolution of position-sensitive detectors for neutron diffraction experiments from 1966 to 1982 in the Nuclear Centre of Grenoble*. *Position-sensitive detection of thermal neutrons,* edited by P. Convert & J. B. Forsyth, pp. 294–301. London: Academic Press.

Schaefer, W., Naday, I. & Will, G. (1983). *Neutron powder diffractometry with the linear position-sensitive scintillation detector*. *Position-sensitive detection of thermal neutrons*, edited by P. Convert & J. B. Forsyth, pp. 209–214. London: Academic Press.

Strauss, M. G., Brenner, R., Chou, H. P., Schultz, A. J. & Roche, C. T. (1983). *Spatial resolution of neutron position scintillation detectors*. *Position-sensitive detection of thermal neutrons,* edited by P. Convert & J. B. Forsyth, pp. 175–187. London: Academic Press.

Strauss, M. G., Brenner, R., Lynch, F. J. & Morgan, C. B. (1981). *2-D position-sensitive scintillation detector for neutrons*. *IEEE Trans. Nucl. Sci.* **28**(1), 800–806.

Thomas, P. (1972). *Production of sensitive converter screens for thermal neutron diffraction patterns*. *J. Appl. Cryst.* **5**, 373–374.

Whaling, W. (1958). *The energy loss of charged particles in matter*. *Handbuch der Physik,* Vol. 34. *Corpuscles and radiation in matter II*, edited by S. Flugge, pp. 193–217. Berlin: Springer-Verlag.

Windsor, C. G. (1981). *Pulsed neutron scattering*. London: Taylor and Francis.

Wolf, R. S. (1974). *Measurement of the gas constants for various proportional counter gas mixtures*. *Nucl. Instrum. Methods*, **115**, 461–463.

7.4.2

Bachmann, R., Kohler, H., Schulz, H. & Weber, H. (1985). *Structure investigation of a CaF_2-crystal with synchrotron radiation*. *Acta Cryst.* A**41**, 35–40.

Cooper, M. J. (1971). *The evaluation of thermal diffuse scattering of neutrons for a one velocity model*. *Acta Cryst.* A**27**, 148–157.

Dorner, B., Burkel, E., Illini, Th. & Peisl, J. (1987). *First measurement of a phonon dispersion curve by inelastic X-ray scattering*. *Z. Phys. B*, **69**, 179–183.

Helmholdt, R. B., Braam, A. W. M. & Vos, A. (1983). *Improved corrections for thermal diffuse scattering*. *Acta Cryst.* A**39**, 90–94.

Helmholdt, R. B. & Vos, A. (1977). *Errors in atomic parameters and electron density distributions due to thermal diffuse scattering of X-rays*. *Acta Cryst.* A**33**, 38–45.

International Tables for Crystallography (1992). Vol. B. *Reciprocal space*, edited by U. Shmueli. Dordrecht: Kluwer.

Jahn, H. A. (1942). *Diffuse scattering of X-rays by crystals*. *The Faxen–Waller theory and the surfaces of isodiffusion for cubic crystals*. *Proc R. Soc. London Ser. A*, **179**, 320–340; **180**, 476–483.

James, R. W. (1962). *The optical principles of the diffraction of X-rays*. London: Bell.

Krec, K. & Steiner, W. (1984). *Investigation of a silicon single crystal by means of the diffraction of Mössbauer radiation*. *Acta Cryst.* A**40**, 459–465.

Krec, K., Steiner, W., Pongratz, P. & Skalicky, P. (1984). *Separation of elastically and inelastically scattered γ-radiation by Mössbauer diffraction*. *Acta Cryst.* A**40**, 465–468.

Merisalo, M. & Kurittu, J. (1978). *Correction of integrated Bragg intensities for anisotropic thermal scattering*. *J. Appl. Cryst.* **11**, 179–183.

Popa, N. C. & Willis, B. T. M. (1994). *Thermal diffuse scattering in time-of-flight diffractometry*. *Acta Cryst.* A**50**, 57–63.

7.4.2 (*cont.*)

Rouse, K. D. & Cooper, M. J. (1969). *The correction of measured integrated Bragg intensities for anisotropic thermal diffuse scattering*. *Acta Cryst*. A**25**, 615–621.

Sakata, M., Stevenson, A. W. & Harada, J. (1983). *G-TDSCOR: one-phonon TDS corrections for measured integrated Bragg intensities*. *J. Appl. Cryst*. **16**, 154–156.

Stevens, E. D. (1974). *Thermal diffuse scattering corrections for single-crystal integrated intensity measurements*. *Acta Cryst*. A**30**, 184–189.

Stevenson, A. W. & Harada, J. (1983). *The consequences of the neglect of TDS correction for temperature parameters*. *Acta Cryst*. A**39**, 202–207.

Suortti, P. (1980). *Powder TDS and multiple scattering*. *Accuracy in powder diffraction*, edited by S. Block & C. R. Hubbard. *Natl Bur. Stand. (US) Spec. Publ*. No. 567, pp. 8–12.

Voigt, W. (1910). *Lehrbuch der Kristallphysik*. Leipzig: Teubner.

Willis, B. T. M. (1970). *The correction of measured neutron structure factors for thermal diffuse scattering*. *Acta Cryst*. A**26**, 396–401.

Willis, B. T. M., Carlile, C. J. & Ward, R. C. (1986). *Neutron diffraction from single-crystal silicon: the dependence of the thermal diffuse scattering on the velocity of sound*. *Acta Cryst*. A**42**, 188–191.

Wooster, W. A. (1962). *Diffuse X-ray reflections from crystals*. Oxford: Clarendon Press.

7.4.3

Åberg, T. & Tulkki, J. (1985). *Inelastic X-ray scattering including resonance phenomena*. *Atomic inner shell physics*, edited by B. Crasemann, Chap. 10. New York: Plenum.

Bannett, Y. B. & Freund, I. (1975). *Resonant X-ray Raman scattering*. *Phys. Rev. Lett*. **34**, 372–376.

Bewilogua, L. (1931). *Incoherent scattering of X-rays*. *Phys. Z.* **32**, 740–744.

Biggs, F., Mendelsohn, L. B. & Mann, J. B. (1975). *Hartree Fock Compton profiles for the elements*. *At. Data Nucl. Data Tables*, **16**, 201–309.

Bloch, B. J. & Mendelsohn, L. B. (1974). *Atomic L-shell Compton profiles and incoherent scattering factors: theory*. *Phys. Rev. A*, **9**, 129–155.

Bloch, F. (1934). *Contribution to the theory of the Compton line shift*. *Phys. Rev*. **46**, 674–687.

Blume, M. & Gibbs, D. (1988). *Polarisation dependence of magnetic X-ray scattering*. *Phys. Rev. B*, **37**, 1779–1789.

Brown, W. D. (1966). *Cross-sections for coherent/incoherent X-ray scattering*. Reports D2-125136-1 and 125137-1. Boeing Co.

Bushuev, V. A. & Kuz'min, R. N. (1977). *Inelastic scattering of X-ray and synchrotron radiation in crystals, coherent effects in inelastic scattering*. *Sov. Phys. Usp*. **20**, 406–431.

Cooper, M. J. (1985). *Compton scattering and electron momentum determination*. *Rep. Prog. Phys*. **48**, 415–481.

Cromer, D. T. (1969). *Compton scattering factors for aspherical free atoms*. *J. Chem. Phys*. **50**, 4857–4859.

Cromer, D. T. & Mann, J. B. (1967). *Compton scattering factors for spherically symmetric free atoms*. *J. Chem. Phys*. **47**, 1892–1893.

Currat, R., DeCicco, P. D. & Weiss, R. J. (1971). *Impulse approximation in Compton scattering*. *Phys. Rev. B*, **4**, 4256–4261.

Eisenberger, P. & Platzman, P. M. (1970). *Compton scattering of X-rays from bound electrons*. *Phys. Rev. A*, **2**, 415–423.

Eisenberger, P., Platzman, P. M. & Winick, M. (1976). *Resonant X-ray Raman scattering studies using synchrotron radiation*. *Phys. Rev. B*, **13**, 2377–2380.

Fermi, E. (1928). *Statistical methods of investigating electrons in atoms*. *Z. Phys*. **48**, 73–79.

Gavrila, M. & Tugulea, M. N. (1975). *Compton scattering by L shell electrons*. *Rev. Roum. Phys*. **20**, 209–230.

Hubbell, J. H., Veigele, W. J., Briggs, E. A., Brown, R. T., Cromer, D. T. & Howerton, R. J. (1975). *Atomic form factors, incoherent scattering functions and photon scattering cross-sections*. *J. Phys. Chem. Ref. Data*, **4**, 471–538.

Jauch, J. M. & Rohrlich, F. (1976). *The theory of photons and electrons*. Berlin: Springer-Verlag.

Klein, O. & Nishina, Y. (1929). *Uber die Streuung von Strahlung durch freie Electronen nach der neuen relativistichers Quantendynamik von Dirac*. *Z. Phys*. **52**, 853–868.

Lipps, F. W. & Tolhoek, H. A. (1954). *Polarisation phenomena of electrons and photons I and II*. *Physica (Utrecht)*, **20**, 85–98, 395–405.

Lovesey, S. W. (1993). *Photon scattering by magnetic solids*. *Rep. Prog. Phys*. **56**, 257–326.

Manninen, S., Paakkari, T. & Kajantie, K. (1976). *Gamma ray Compton profile of aluminium*. *Philos. Mag*. **29**, 167–178.

Pattison, P. & Schneider, J. R. (1979). *Test of the relativistic 1s wavefunction in Au and Pb using experimental Compton profiles*. *J. Phys. B*, **12**, 4013–4019.

Pratt, R. H. & Tseng, H. K. (1972). *Behaviour of electron wavefunctions near the atomic nucleus and normalisation screening theory in the atomic photoeffect*. *Phys. Rev. A*, **5**, 1063–1072.

Ribberfors, R. (1975). *Relationship of the relativistic Compton cross-section to the momentum distribution of bound electron states. II. Effects of anisotropy and polarisation*. *Phys. Rev. B*, **12**, 2067–2074, 3136–3141.

Ribberfors, R. (1983). *X-ray incoherent scattering total cross-sections and energy absorption cross-sections by means of simple calculation routines*. *Phys. Rev. A*, **27**, 3061–3070.

Ribberfors, R. & Berggren, K.-F. (1982). *Incoherent X-ray scattering functions and cross sections by means of a pocket calculator*. *Phys. Rev. A*, **26**, 3325–3333.

Schaupp, D., Czerwinski, H., Smend, F., Wenskus, R., Schumacher, M., Millhouse, A. H. & Strauss, S. (1984). *Resonant Raman scattering of synchrotron X-rays by neodymium: observation of fine structure in K-L-RRS and of K-N-RRS*. *Z. Phys. A*, **319**, 1–7.

Slater, J. C. (1937). *Wavefunctions in a periodic crystal*. *Phys. Rev*. **51**, 846–851.

Sparks, C. J. (1974). *Inelastic resonance emission of X-rays: anomalous scattering associated with anomalous dispersion*. *Phys. Rev. Lett*. **33**, 262–265.

Thomas, L. H. (1927). *Calculation of atomic fields*. *Proc. Cambridge Philos. Soc*. **33**, 542–548.

Veigele, W. J. (1967). *Research of X-ray scattering cross sections: final report*. Report KN-379-67-3(R). Kaman Sciences Corp.

Waller, I. & Hartree, D. R. (1929). *Intensity of total scattering of X-rays*. *Proc. R. Soc. London Ser. A*, **124**, 119–142.

Williams, B. G. (1977). *Compton scattering*. New York: McGraw-Hill.

7.4.4

Brown, G. S. & Lindau, I. (1986). Editors, *Synchrotron radiation instrumentation*. Proceedings of the International Conference on X-ray and VUV Synchrotron Radiation Instrumentation. *Nucl. Instrum. Methods*, A**246**, 511–595.

Mathieson, A. McL. (1985). *Small-crystal X-ray diffractometry with a crystal ante-monochromator*. *Acta Cryst.* A**41**, 309–316.

Matsushita, T. & Hashizume, H. (1983). *Handbook of synchrotron radiation*, Vol. I, edited by E. E. Koch, pp. 261–314. Amsterdam: North-Holland.

Matsushita, T. & Kaminaga, U. (1980). *A systematic method of estimating the performance of X-ray optical systems for synchrotron radiation. I. Description of various optical elements in position-angle space for ideally monochromatic X-rays*. *J. Appl. Cryst.* **13**, 465–471; *II. Treatment in position–angle–wavelength space*. *J. Appl. Cryst.* **13**, 472–478.

Suortti, P. (1980). *Components of the total X-ray scattering*. *Accuracy in powder diffraction,* edited by S. Block & C. R. Hubbard, pp. 1–20. *Natl Bur. Stand. (US) Spec. Publ.* No. 567.

Suortti, P. (1985). *Parallel beam geometry for single-crystal diffraction*. *J. Appl. Cryst.* **18**, 272–274.

Suortti, P., Hastings, J. B. & Cox, D. E. (1985). *Powder diffraction with synchrotron radiation. I. Absolute measurements*. *Acta Cryst.* A**41**, 413–416.

Suortti, P. & Jennings, L. D. (1977). *Accuracy of structure factors from X-ray powder intensity measurements*. *Acta Cryst.* A**33**, 1012–1027.

Thomlinson, W. & Williams, G. P. (1984). Editors. *Synchrotron radiation instrumentation 3*. Proceedings of the Third National Conference on Synchrotron Radiation Instrumentation. *Nucl. Instrum. Methods*, **222**, 215–278.

7.5

Abramowitz, M. & Stegun, I. A. (1964). *Handbook of mathematical functions*. National Bureau of Standards Publication AMS 55.

Boer, J. L. de (1982). *Statistics of recorded counts*. *Crystallographic statistics*, edited by S. Ramaseshan, M. F. Richardson & A. J. C. Wilson, pp. 179–186. Bangalore: Indian Academy of Sciences.

Eastabrook, J. N. & Hughes, J. W. (1953). *Elimination of dead-time corrections in monitored Geiger-counter X-ray measurements*. *J. Sci. Instrum.* **30**, 317–320.

French, S. & Wilson, K. (1978). *On the treatment of negative intensity observations*. *Acta Cryst.* A**34**, 517–525.

Grant, D. F. (1973). *Single-crystal diffractometer data: the on-line control of the precision of intensity measurement*. *Acta Cryst.* A**29**, 217.

Hirshfeld, F. L. & Rabinovich, D. (1973). *Treating weak reflexions in least-squares calculations*. *Acta Cryst.* A**29**, 510–513.

Killean, R. C. G. (1967). *A note on the a priori estimation of R factors for constant-count-per-reflection diffractometer experiments*. *Acta Cryst.* **23**, 1109–1110.

Killean, R. C. G. (1972). *The a priori optimization of diffractometer data to achieve the minimum average variance in the electron density*. *Acta Cryst.* A**28**, 657–658.

Killean, R. C. G. (1973). *Optimization of scan procedure for single-crystal X-ray diffraction intensities*. *Acta Cryst.* A**29**, 216–217.

Mack, M. & Spielberg, N. (1958). *Statistical factors in X-ray intensity measurements*. *Spectrochim. Acta*, **12**, 169–178.

Mackenzie, J. K. & Williams, E. J. (1973). *The optimum distribution of counting times for determining integrated intensities with a diffractometer*. *Acta Cryst.* A**29**, 201–204.

Olkha, G. S. & Rathie, P. N. (1971). *On a generalized Bessel function and an integral transform*. *Math. Nachr.* **51**, 231–240.

Paciorek, W. A. & Chapuis, G. (1994). *Generalized Bessel functions in incommensurate structure analysis*. *Acta Cryst.* A**50**, 194–203.

Parrish, W. (1956). *X-ray intensity measurements with counter tubes*. *Philips Tech. Rev.* **17**, 206–221.

Prince, E. & Nicholson, W. L. (1985). *The influence of individual reflections on the precision of parameter estimates in least squares refinement*. *Structure & statistics in crystallography*, edited by A. J. C. Wilson, pp. 183–195. Guilderland, NY: Adenine Press.

Shmueli, U. (1993). Editor. *International tables for crystallography*. Vol. B. *Reciprocal space*. Dordrecht: Kluwer.

Shoemaker, D. P. (1968). *Optimization of counting times in computer-controlled X-ray and neutron single-crystal diffractometry*. *Acta Cryst.* A**24**, 136–142.

Shoemaker, D. P. & Hamilton, W. C. (1972). *Further remarks concerning optimization of counting times in single-crystal diffractometry: rebuttal to Killean; consideration of background counting and slewing times*. *Acta Cryst.* A**28**, 408–411.

Skellam, J. G. (1946). *The frequency distribution of the difference between two Poisson values belonging to different populations*. *J. R. Stat. Soc.* **109**, 296.

Szabó, P. (1978). *Optimization of the measuring time in diffraction intensity measurements*. *Acta Cryst.* A**34**, 551–553.

Thomsen, J. S. & Yap, F. Y. (1968). *Simplified method of computing centroids of X-ray profiles*. *Acta Cryst.* A**24**, 702–703.

Werner, S. A. (1972*a*). *Choice of scans in X-ray diffraction*. *Acta Cryst.* A**28**, 143–151.

Werner, S. A. (1972*b*). *Choice of scans in neutron diffraction*. *Acta Cryst.* A**28**, 665–669.

Wilson, A. J. C. (1967). *Statistical variance of line-profile parameters. Measures of intensity, location and dispersion*. *Acta Cryst.* **23**, 888–898.

Wilson, A. J. C. (1978). *On the probability of measuring the intensity of a reflection as negative*. *Acta Cryst.* A**34**, 474–475.

Wilson, A. J. C. (1980). *Relationship between 'observed' and 'true' intensity: effect of various counting modes*. *Acta Cryst.* A**36**, 929–936.

Wilson, A. J. C., Thomsen, J. S. & Yap, F. Y. (1965). *Minimization of the variance of parameters derived from X-ray powder diffractometer line profiles*. *Appl. Phys. Lett.* **7**, 163–165.

Wright, E. M. (1933). *On the coefficients of power series having exponential singularities*. *J. London Math. Soc.* **8**, 71–79.

Zevin, L. S., Umanskii, M. M., Kheiker, D. M. & Panchenko, Yu. M. (1961). *K voprosu o difraktometricheskikh priemah pretsizionnyh izmerenii elementarnyh yacheek*. *Kristallografiya*, **6**, 348–356.